

Contents lists available at ScienceDirect

International Journal of Plasticity

journal homepage: www.elsevier.com/locate/ijplas





On the torsional and coupled torsion-tension/compression behavior of magnesium alloy solid rod: A crystal plasticity evaluation

Huamiao Wang a,b,* , Xiaodan Zhang a,b , Wei Wu c , Peter K. Liaw c , Ke An d , Qin Yu e,* , Peidong Wu f

- a State Key Laboratory of Mechanical Systems and Vibration, Shanghai Jiao Tong University, Shanghai 200240, China
- ^b Materials Genome Initiative Center, Shanghai Jiao Tong University, Shanghai 200240, China
- ^c Department of Materials Science Engineering, The University of Tennessee, Knoxville, TN 37996 USA
- ^d Neutron Scattering Division, Oak Ridge National Laboratory, Oak Ridge, TN 37831, USA
- ^e Materials Sciences Division, Lawrence Berkeley National Laboratory, Berkeley, CA 94720, USA
- f Department of Mechanical Engineering, McMaster University, Hamilton L8S 4L7, Ontario, Canada

ARTICLE INFO

Keywords: Coupled torsion-tension Multiaxial Magnesium alloys Twinning Crystal plasticity

ABSTRACT

Extensive attention has been paid to magnesium (Mg) alloys considering their potential as lightweight structural materials. However, it is still challenging to process and manufacture Mg materials that carry high strength and good ductility. This issue mainly arises from a lack of understanding toward the anisotropic mechanical behavior of Mg alloys in response to large deformation in a multiaxial stress state, which is unavoidably in existence under various material processing routes. In this regard, we seek to understand the torsional and coupled torsiontension/compression behaviors of a magnesium alloy subject to large-strain deformation. The elastic viscoplastic self-consistent (EVPSC) model, which incorporates the twinning-detwinning (TDT) scheme and takes a torsion-specific finite element (TFE) approach, was employed to illuminate the inhomogeneous and multiaxial features of the torsional deformation in the AZ31 Mg alloy subjected to free/fixed-end torsion and coupled torsion-tension/compression. Experimental validation was conducted by characterizing the mechanical responses of the torsional specimens under the loading paths of free-end torsion and coupled torsion-tension. Our model successfully captures the Swift effect along with the shear texture, which is hardly predicted by conventional constitutive models. In addition, our model reveals that twinning is nearly equally active under free-/fixed-end torsion, while twinning under coupled torsion-tension and torsion-compression is promoted and suppressed, respectively. The comparison between the simple shear and pure torsion by simulation demonstrates that the significant bulk stress existing within the torsional rod is ascribed to the strong interaction between the cylindrical elements in the EVPSC model. As a final thought, we believe that the TFE-EVPSC-TDT model not only highlights the inhomogeneous and multiaxial features underlying the torsional and coupled torsion-tension/compression behaviors of the Mg alloy solid rod, but more significantly, can be used as a numerical tool for designing/tuning gradient twinning structures that may lead to optimized properties of Mg alloys.

E-mail addresses: wanghm02@sjtu.edu.cn (H. Wang), qin.yu.unr@gmail.com (Q. Yu).

^{*} Corresponding author.

1. Introduction

Owing to the high specific strength (normalized by the density), magnesium (Mg) alloys have gained considerable attention as structural materials for weight reduction in automotive and aerospace industries (Barnett, 2007; Pollock, 2010; Sun et al., 2019). However, Mg alloys usually exhibit strong mechanical anisotropy and poor ductility/formability at room temperature. This feature is originated from the limited slip/twin systems in the hexagonal-close-packed (hcp) crystallographic structure (Agnew and Duygulu, 2005; Indurkar et al., 2020). The anisotropic mechanical properties coupled with the existence of a multiaxial stress state under various material processing routes have imposed unparalleled challenges for optimizing the mechanical properties of Mg materials.

Tremendous efforts have been taken to study the deformation behavior of *hcp* Mg alloys that undergo homogenous deformation in response to uniaxial tension and compression (Agnew and Duygulu, 2005; Lou et al., 2007; Wu et al., 2008; Wang et al., 2010a,b; 2012a; 2016a,b; 2018; 2020a; Chapuis and Drivers, 2011; Khan et al., 2011; Popova et al., 2015; Zhou et al., 2016; Tang et al., 2019; Zecevic et al., 2019; Zhang et al., 2021a). As highlights, Agnew and Duygulu (2005), Lou et al. (2007), and Proust et al. (2009) studied the deformation of an Mg alloy, AZ31B, rolled sheets by means of the in-plane compression and tension and the through-thickness compression. Lou et al. (2007) and Wang et al. (2015a) carefully examined the cyclic shear deformation of an AZ31 rolled plate and characterized the corresponding twinning/detwinning activity. Oppedal et al. (2011) and Qiao et al. (2017) inspected the strain-hardening behavior of an Mg alloy, AM30, bar subjected to tension along directions oriented at different tilt angles with respect to the extrusion direction (ED). Similarly, Guo et al. (2015) and Wang et al. (2020b) investigated the anisotropic behavior of a hot-rolled Mg alloy, AZ31, loaded at different tilt angles relative to the rolling direction (RD). Results have shown that the anisotropic mechanical behavior of Mg materials, which involve twinning activities, requires constitutive modeling with better predictability.

Compared to the tension/compression loading path, relatively few studies have been dedicated to studying the shear deformation of Mg alloys; most of the prior work focused on shear deformation involved in severe plastic deformation (SPD) processing (Beyerlein and Tóth, 2009; Chino et al., 2008; Huang et al., 2008). Simple shear and pure torsion are two common tests to characterize the shear response of materials. For Mg alloys, the simple shear experiment is less frequently employed due to the difficulties in sustaining a homogenous shear deformation and attaining a large strain without fracture. For example, the shear strain at fracture for an AZ31B Mg alloy sheet tested under the simple shear is ~0.22, being only half of that obtained in a torsion test for an AZ31B Mg alloy at room temperature (Beausir et al., 2009; Guo et al., 2013). For that reason, torsion experiment was regularly taken to study the roles of texture, dislocation slip, and twinning on the shear response of Mg alloys (Lou et al., 2007; Barnett, 2001; Balasubramanian and Anand, 2002; Beausir et al., 2009; Wang et al., 2010a; Zhang et al., 2011; Wu et al., 2012; Kang et al., 2012, Guo et al., 2013; Wang et al., 2013b; Zhang et al., 2020b.

Other than simple shear or pure torsion, various processing routes often involve multiaxial stress states. Some prior work investigated the biaxial tension and in-plane compression deformation of Mg alloys by experiments and simulations (Andar et al., 2012; Hama and Takuda, 2012; Steglich et al., 2012). In addition, multiaxial fatigue properties of Mg alloys were studied by coupled axial-torsion experiments using thin-walled tubular specimens (Albinmousa et al., 2011; Bentachfine et al., 1996; Xiong et al., 2012; Zhang et al., 2011). However, to avoid buckling of thin-walled tubular specimens, small stress/strain amplitudes were employed in the fatigue experiments (Zhang et al., 2011). Therefore, the multiaxial response of Mg alloy under large-strain deformation remains relatively unknown. To fill this gap, we intend to understand the torsional behaviors of Mg alloys through crystal plasticity modeling and experimental validation by carrying out free-end torsion and coupled torsion-tension experiments on Mg alloy solid rod specimens, where bulking can be prevented at large shear strain.

While direct measurement of mechanical responses is important, only a limited number of loading paths is experimentally investigated due to the inadequate resources. However, a numerical simulation based on the crystal plasticity model is particularly useful with regard to their almost unlimited restriction on the simulation cases. More significantly, the crystal plasticity model enables the revealing of the deformation mechanisms. Due to the computational efficiency and feasibility, mean-field crystal-plasticity models are widely taken over the full-field models (Clausen et al., 2008; Abdolvand et al., 2011; 2015; Abdolvand and Daymond, 2012; Dawson et al., 2018; Wang et al., 2018; Ma et al., 2019; Xin et al., 2019; Paramatmuni and Dunne, 2020; Sahoo et al., 2020; Ganesan et al., 2021). However, the mean-field models are only suitable for modeling homogenous deformation of a material point. Unlike the homogenous deformation under uniaxial tension/compression or simple shear, the stress and strain fields distribute inhomogeneously in the material under torsional deformation. To consider such torsional nonuniformity, the full-field technique must be adopted. For this reason, we have developed a torsion-specific finite element approach, which has been proved highly efficient and effective to account for the deformation inhomogeneity in torsional problem (Chinoet al., 2008; Beausir et al., 2009; Wang et al., 2010b; 2015a; Zhang et al., 2011). In addition, the activity of the extension twin is difficult to be modeled. Tremendous efforts were devoted to the twinning schemes, e.g., the predominant twin reorientation (PTR) (Lebensohn and Tomé, 1993; Van Houtte, 1978), composite grain (CG) scheme (Proust et al., 2007), all twin variant (ATV) (Sahoo et al., 2020), and twinning and detwinning (TDT) scheme (Wang et al., 2012a) and so on. Among them, the TDT scheme (Wang et al., 2012a; 2013b) is superior in dealing with twinning and detwinning, which has been proved to give optimized prediction performance (Wang et al., 2015a,b; 2016a; Qiao et al., 2015; Ma et al., 2019; Zhang et al., 2021b). This torsion-specific finite element (TFE) approach and the elastic visco-plastic self-consistent (EVPSC) polycrystal framework coupled with the twinning and detwinning (TDT) scheme will be employed to interpret the characteristic deformation in our Mg alloy solid rod under free/fixed-end pure torsion and coupled torsion-tension/compression loading. The crystal plasticity approach taken in our work, which is validated by the available experimental results, is likely the first effort to understand the deformation mechanisms underlying the coupled torsion-tension/compression behaviors of Mg alloys.

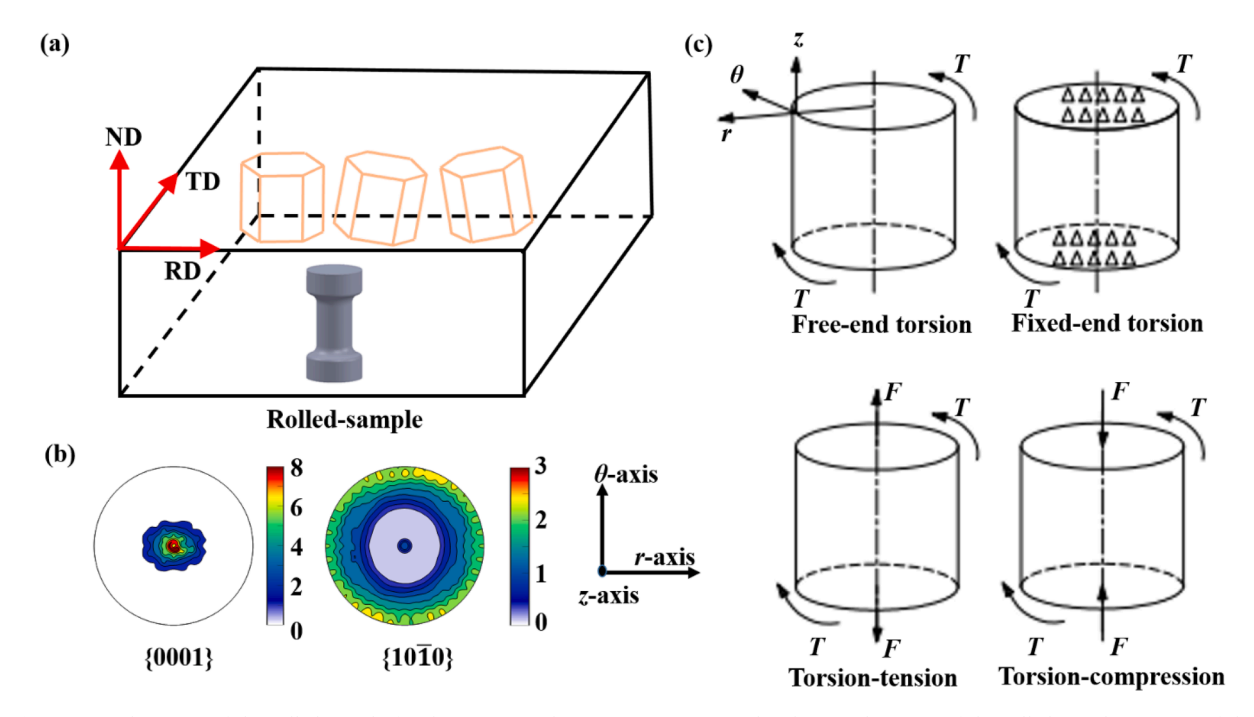


Fig. 1. (a) Schematics of the rolled-sample for the torsion and torsion-tension tests. (b) The initial texture of the rolled-sample in terms of the $\{0001\}$ and $\{10\overline{1}0\}$ pole figures plotted in the $\theta-r$ plane. (c) Simulations under four torsional loading paths, *i.e.* free/fixed-end pure torsion, and coupled torsion-tension/compress. Experimental validations were performed only with the free-end torsion and the coupled torsion-tension.

2. Experimental procedure

The material studied was a rolled AZ31B [Mg-3.0Al-1.0 Zn, weight percent (wt.%)] plate (76 mm in thickness) processed with an H24 temper heat treatment, denoted as "rolled-sample" in the following discussions. Uniaxial tension/compression experiments were carried out to calibrate the model parameters using dog-bone cylinder specimens along the rolling direction (RD). In order to validate the torsional behaviors simulated by crystal plasticity modeling, cylindrical dog-bone solid rod specimens were machined with their axial directions (ADs) oriented along the normal direction (ND) (Fig. 1a). The initial length and radius of the gauge section of the cylindrical rods were 20 mm and 5 mm, respectively. Before mechanical loading, the samples were annealed at 345°C for 2 h to remove the residual stress induced by the specimen machining. The average grain size after annealing was about 40 μ m. Neutron diffraction was used to measure the initial texture, which exhibits an intense basal texture (Fig. 1b). In the current work, the rolled-sample was tested under free-end torsion and coupled torsion-tension. All tests were conducted at room temperature using an axial-torsion MTS load frame. More details of the testing specimen and the mechanical experiments can be referred to Appendix A.

3. Problem formulation and method

3.1. EVPSC-TDT model

Since the EVPSC-TDT model has been reported elsewhere (Wang et al., 2010c; 2012a; Wang et al., 2013a,b), only a brief description is provided here. The strain rate, $\dot{\varepsilon}_{ij}$, consists of elastic and plastic components, $\dot{\varepsilon}_{ij}^{p}$ and $\dot{\varepsilon}_{ij}^{p}$, in a single crystal. For the Mg alloy, the plastic deformation originates from both slip and twinning:

$$\dot{\varepsilon}_{ij} = \dot{\varepsilon}^e_{ij} + \dot{\varepsilon}^p_{ij} = M^e_{ijkl} \dot{\sigma}_{kl} + \sum_{\alpha} \dot{\gamma}^{\alpha} P^{\alpha}_{ij} \tag{1}$$

where M^e_{ijkl} is the elastic compliance matrix, $\dot{\gamma}^\alpha$ is the shear rate, and $P^\alpha_{ij} = (s^\alpha_i n^\alpha_j + n^\alpha_i s^\alpha_j)/2$ is the Schmid tensor for a slip/twinning system α , with s^α_i and n^α_i being the unit vectors of the slip/twinning direction and the plane normal of the slip/twinning system, respectively. The driving force for the shear rate $\dot{\gamma}^\alpha$ in both slip and twinning systems is the resolved shear stress (RSS), $\tau^\alpha = \sigma_{ij} P^\alpha_{ij}$, where σ_{ij} is the Cauchy stress. For a slip system, α , the shear rate can be expressed as

$$\dot{\gamma}^{\alpha} = \dot{\gamma}_0 \left| \frac{\tau^{\alpha}}{\tau_{\alpha_r}^a} \right|^{\frac{1}{m}} sgn(\tau^{\alpha}) \tag{2}$$

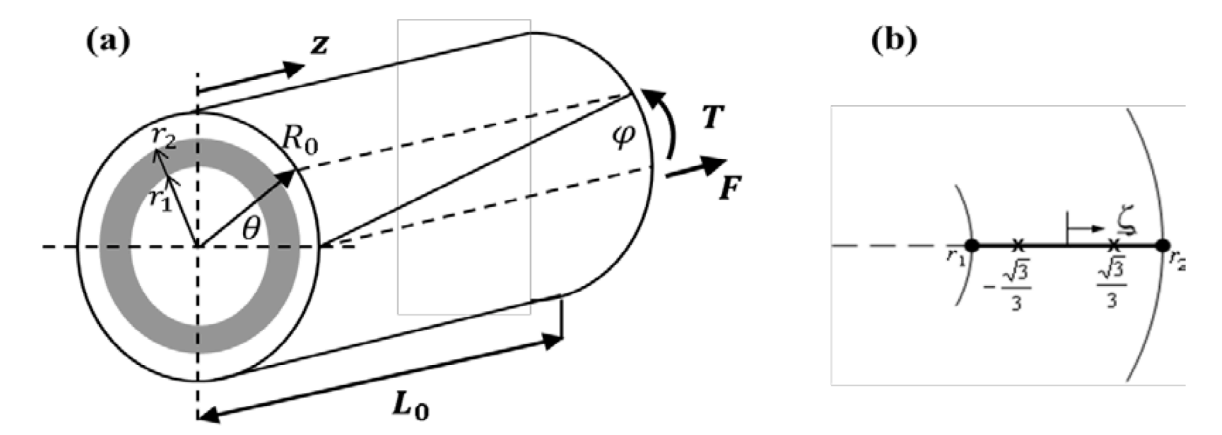


Fig. 2. Schematic of the torsion-specific finite element: (a) definition of the cylindrical tube element with inner and outer radii of r_1 and r_2 ; and (b) material sampling points (×).

in terms of the reference shear rate, $\dot{\gamma}_0$, the critical resolved shear stress (CRSS), τ^a_{cr} , and the strain rate sensitivity, m.

The TDT scheme introduces six twin variants (for the extension twin system of Mg alloy) in each parent grain where the stresses in both the matrix and the twin drive the events of twinning and de-twinning. A twin-free grain starts twinning by twin nucleation (TN) if the resolved shear stress (RSS) is along the twin shear direction and reaches a threshold value. A new twin is treated as a new grain, which is embedded in the effective medium as a new inclusion. The orientation of the new grain is obtained through the twin/matrix orientation relation, *i.e.*, the rotation tensor $Q = 2n^{\alpha}n^{\alpha} - 1$, where n^{α} is the plane normal of the twinning variant α . The nucleated twins will grow by the mechanism of twin growth (TG), which is driven by the stresses within both the parent grain and the twin. The shear rates and the corresponding rates of the volume fractions for the matrix and twin are, respectively, expressed as

$$\dot{\gamma}_{M}^{\alpha} = \begin{cases} \dot{\gamma}_{0} \left| \frac{\tau^{\alpha}}{\tau_{cr}^{\alpha}} \right|^{\frac{1}{m}} & \tau^{\alpha} > 0 \\ 0 & \tau^{\alpha} \le 0 \end{cases}, \quad \dot{f}_{M}^{\alpha} = \frac{\left| \dot{\gamma}_{M}^{\alpha} \right|}{\gamma^{n_{v}}}$$

$$(3)$$

$$\dot{\gamma}_{T}^{\alpha} = \begin{cases} -\dot{\gamma}_{0} \left| \frac{\tau^{\alpha}}{\tau_{cr}^{\alpha}} \right|^{\frac{1}{m}} & \tau^{\alpha} < 0 \\ 0 & \tau^{\alpha} \ge 0 \end{cases}, \quad \dot{f}_{T}^{\alpha} = \frac{\left| \dot{\gamma}_{T}^{\alpha} \right|}{\gamma^{tw}} \end{cases}$$

$$(4)$$

where \hat{f}_M^a and \hat{f}_T^a are the rates of volume fraction of the matrix and twin, respectively. γ^{tw} is the characteristic twinning shear, which is 0.129 for Mg alloys. The net change of the TVF corresponding to the twinning system, α , is:

$$\dot{f}^{a} = f^{M} f_{M}^{a} + f^{\alpha} f_{T}^{a} \tag{5}$$

where $f^{M} = 1 - f^{tw} = 1 - \sum_{\alpha} f^{\alpha}$ is the volume fraction of the matrix. Twinning is terminated within a grain if the TVF f^{tw} reaches a threshold value, V^{th} , which is a function of the accumulated twin fraction, V^{acc} , and the effective twinned fraction, V^{eff} (i.e. the volume fraction of the twin-exhausted grains),

$$V^{th} = \min\left(1.0, A_1 + \frac{A_2 V^{eff}}{V^{acc}}\right)$$
 (6)

where A_1 and A_2 are two governing parameters.

For the slip/twinning system, α , the evolution of the CRSS, τ_{cr}^{α} , can be expressed as:

$$\dot{\tau}_{cr}^{\alpha} = \frac{d\hat{\tau}^{a}}{d\gamma_{accu}} \sum_{\beta} h^{\alpha\beta} |\dot{\gamma}^{\beta}| \tag{7}$$

where $\gamma_{accu} = \sum_{\alpha} \int_{\alpha}^{\gamma^{\alpha}} dt$ is the accumulated shear strain in the grain, and $h^{\alpha\beta}$ are the latent hardening-coupling coefficients, which empirically account for the obstacles imposed on the system, α , associated with the system, β . $\hat{\tau}^a$ is the threshold stress and is defined as:

$$\widehat{\tau}^a = \tau_0^a + \left(\tau_1^a + h_1^a \gamma_{accu}\right) \left(1 - \exp\left(-\frac{h_0^a \gamma_{accu}}{\tau_1^a}\right)\right) \tag{8}$$

where τ_0 and $\tau_0 + \tau_1$ are the initial and back-extrapolated CRSSes, respectively. h_0 and h_1 are the initial and asymptotic hardening rates, respectively.

The TDT scheme is used in conjunction with the EVPSC model, which treats grains as inclusions embedded in a homogeneous effective medium (HEM) consisted of all the grains at a material point. The single crystal constitutive rule of the TDT scheme and the self-consistency criteria based on the Eshelby inclusion formalism are solved simultaneously (Eshelby, 1957; Wang et al., 2010c; 2013b). This ensures that the grain-level stress and strain rates are consistent with the boundary conditions imposed on the HEM. Different linearization schemes exist for the self-consistent models, where the Affine self-consistent scheme gives the best overall performance based on a series of evaluations (Wang et al., 2010a-c; Wang et al., 2012b, 2018; Qiao et al., 2015; Masson et al., 2000; Lebensohn et al., 2007; Ma et al., 2019). Consequently, the EVPSC-TDT model with the Affine scheme was employed here to study the torsional and torsion-tension/compression coupling behaviors of Mg alloys.

3.2. Torsion-specific finite-element approach

Fig. 2 shows a schematic of the torsion-specific finite element. As shown in Fig. 2a, the initial radius and length of the cylindrical solid rod are R_0 and L_0 , respectively. The rod is subjected to a twist, φ , and an axial displacement, U. The corresponding torque and the axial force are T and F, respectively. The two end surfaces of the rod are assumed to remain planar and perpendicular to the axial direction so that any cross-section of the rod remains planar. The lateral surface of the rod is traction-free, and the behavior remains axisymmetric and homogeneous along the axial direction. The rod remains circularly cylindrical with a current radius, R, and current length, L.

A torsion-specific finite-element (TFE) approach (Wu and Van der Giessen, 1991) was adopted to solve the governing equations for the coupled torsion-tension problem. All governing equations are referred to a cylindrical coordinate system with $x = re_r + r\theta e_\theta + ze_z$ with (e_r, e_θ, e_z) being the three orthogonal base vectors. If the initial coordinates of a material point are $x^0 = r_0e_r + \theta_0e_\theta + z_0e_z$, then its current coordinates are:

$$r = r(r_0); \ \theta = \theta_0 + \psi z_0; \ z = \lambda z_0$$
 (9)

Here $\psi = \varphi/L_0$ is the twist per unit length of the rod in the undeformed configuration, and $\lambda = L/L_0 = 1 + U/L_0$ is the stretch in the axial direction. The velocity vector, $\mathbf{v} = d\mathbf{x}/dt = v_i \mathbf{e}_i$, is given with the components, $(\mathbf{v}_i) = (\dot{r}, \mathbf{z}\dot{\psi}/\lambda, \mathbf{z}\dot{\lambda}/\lambda)$. Thus, the components of the strain-rate tensor, $\dot{\mathbf{e}} = \dot{e}_{ij}\mathbf{e}_i \otimes \mathbf{e}_i$, and the spin tensor, $\boldsymbol{\omega} = \omega_{ij}\mathbf{e}_i \otimes \mathbf{e}_i$, can be represented by

$$\dot{\varepsilon}_{11} = \frac{\partial \dot{r}}{\partial r}, \ \dot{\varepsilon}_{22} = \frac{\dot{r}}{r}, \ \dot{\varepsilon}_{33} = \frac{\dot{\lambda}}{\lambda}, \ \dot{\varepsilon}_{23} = \frac{r}{2} \frac{\dot{\psi}}{\lambda}, \ \dot{\varepsilon}_{12} = \dot{\varepsilon}_{13} = 0 \tag{10}$$

$$\omega_{12} = -\frac{z\dot{\psi}}{\lambda}, \ \omega_{23} = \frac{r}{2}\frac{\dot{\psi}}{\lambda}, \ \omega_{13} = 0 \tag{11}$$

The assumptions of the axial homogeneity and the axis-symmetry make the true stress, $\sigma_{ij}e_i \otimes e_j$, only a function of the radius, $\sigma_{ij} = \sigma_{ij}(r)$, with $\sigma_{12} = \sigma_{13} = 0$. The resultant axial force, F, and torque, T, are given by:

$$F = 2\pi \int_{0}^{R} r \sigma_{33} dr; \ T = 2\pi \int_{0}^{R} r^{2} \sigma_{23} dr \tag{12}$$

while the lateral surface is stress-free, $\sigma_{11}(R) = 0$.

This problem can be efficiently solved by the torsion-specific finite elements along the radial direction (Wu and Van der Giessen, 1991). The specific element is a cylindrical tube with an inner radius, r_1 , and outer radius, r_2 , in the deformed configuration (Fig. 2b). The finite element model is composed of n elements. The degrees of freedom for each element are the angle of twist, ψ , the overall axial displacement, U, and the radial nodal displacements. The procedure outlined in Van der Giessen (1987) for the present elements leads to the introduction of two sampling points located at $\xi_{\rm I} = -\frac{\sqrt{3}}{3}(r = r_{\rm I})$ and $\xi_{\rm II} = \frac{\sqrt{3}}{3}(r = r_{\rm II})$, respectively. ξ is a local coordinate and $\xi_{\rm I}$ and $\xi_{\rm II}$ coincide with the Gaussian integration points in this case. The radial velocity at a point ξ within the element is linearly interpolated as $\frac{\dot{r}}{r} = \frac{1}{2} \left[(1 - \xi) \frac{\dot{r}_1}{r_1} + (1 + \xi) \frac{\dot{r}_2}{r_2} \right]$. The element's velocity vector, v^{el} , can be taken in terms of the radial nodal velocities, \dot{r}_1 and \dot{r}_2 , as:

$$\mathbf{v}^{el} = \begin{bmatrix} \dot{r}_1, \dot{r}_2, \dot{\psi}, \dot{\lambda} \\ \dot{r}_1, \dot{r}_2, \dot{\chi}, \dot{\lambda} \end{bmatrix} \tag{13}$$

The element's force vector, F^{el} , dual to v^{el} , such that $F^{el} \cdot v^{el}$ is the rate of work of loads on the element, is given by:

$$F^{el} = [r_1 F_{r1}, r_2 F_{r2}, T^{el}, LF^{el}]$$
(14)

with F_{r1} , F_{r2} , F^{el} , and T^{el} being the inner radial nodal force, the outer radial nodal force, the axial force, and the torque acting on the element, respectively. The total axial force, F, and the torque, T, acting on the rod are obtained by the summation over all elements:

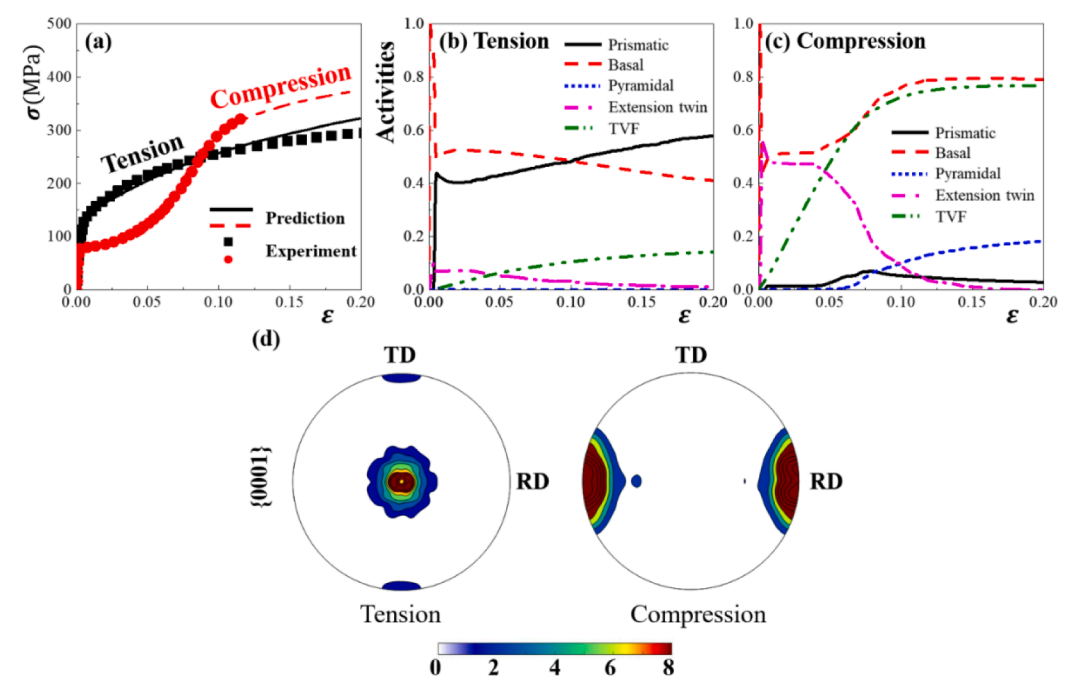


Fig. 3. (a) Experimentally measured (symbols) and simulated (solid and dashed lines) stress-strain curves of the AZ31B plate under uniaxial tension and compression along the RD. Relative activities of various deformation mechanisms and twin volume fractions (TVFs) as a function of the uniaxial strain under (b) tension and (c) compression. (d) The predicted deformation textures under tension and compression at a strain of 0.2 in terms of {0001} pole figure.

$$F = \sum_{el-1}^{n} F^{el}, \ T = \sum_{el-1}^{n} T^{el}$$
 (15)

The governing equations are formulated within a framework using the concept of material sampling points (Van der Giessen, 1987). Together with (10), this leads to the element equilibrium equations of the form:

$$D^T \Sigma = F^{el} \tag{16}$$

The vector, Σ , contains the sampling point stress components, while the matrix, D, depends on the current geometry (Wu and Van der Giessen, 1991). The traction-free lateral surface of the rod requires that radial forces F_{ri} vanish at internal nodes and at the outmost node at r = R. We define the vectors of element stresses and strain-rates as: $\Sigma = v^{\ell} [\dot{\varepsilon}_{11}^{l} \ \dot{\varepsilon}_{22}^{l} \ 2\dot{\varepsilon}_{23}^{l} \ \dot{\varepsilon}_{33}^{l} \ \vdots \ \dot{\varepsilon}_{11}^{ll} \ \dot{\varepsilon}_{22}^{ll} \ 2\dot{\varepsilon}_{23}^{ll} \ \dot{\varepsilon}_{33}^{ll}]^{T}$, where $v^{\ell} = \pi(r_{2}^{2} - r_{1}^{2})L$, $\dot{E} = [\dot{\varepsilon}_{11}^{l} \ \dot{\varepsilon}_{22}^{l} \ 2\dot{\varepsilon}_{23}^{l} \ \dot{\varepsilon}_{33}^{l} \ \vdots \ \dot{\varepsilon}_{33}^{ll} \ \dot{\varepsilon}_{33}^{ll}]^{T} = Dv^{\ell l} = [D_{I} \ D_{II}]^{T}v^{\ell l}$, and

$$D_{i} = \begin{bmatrix} -\left(\xi_{i} - \frac{r_{1}}{b}\right) \left(\xi_{i} + \frac{r_{2}}{b}\right) 0 & 0\\ \frac{\left(1 - \xi_{i}\right)r_{i}^{2}}{2} & \left(1 + \xi_{i}\right)r_{i}^{2}}{2} & 0 & 0\\ 0 & 0 & r_{i}^{2}/L & 1\\ 0 & 0 & 0 & 1 \end{bmatrix} \quad (i = I, II; and b = r_{2} - r_{1})$$

A straightforward time differentiation is used to obtain the equilibrium conditions at the current instant. The following finite element equations for the unknown v^{el} could be obtained by means of the constitutive law (Section 3.1) after elimination of the stress rates:

$$\mathbf{K}\mathbf{v}^{el} = \dot{\mathbf{F}}^{el} + \dot{\mathbf{F}}^{el}_{\cdot \cdot \cdot} \tag{17}$$

The additional force rate, $F_{\nu_{\nu}}^{l}$, represents the viscous terms and can be obtained by the constitutive law (Section 3.1).

The procedure is a linear incremental solution to study the deformation, which is based on a time step Δt and with a simultaneous updating of the configuration. At each time increment, $(\Delta t v^{el})$ is obtained from the global equations assembled for the entire bar:

$$K(\Delta t v^{el}) = \Delta t (\dot{F}^{el} + \dot{F}^{el}_{v}) - (D^{T} \Sigma - F^{el})$$

$$\tag{18}$$

Table 1Values of the parameters associated with the model.

C_{11} =58 GPa; C_{12} =25; C_{13} =20.8; C_{33} =61.2; C_{44} =16.6				$m = 0.05; \dot{\gamma}_0 = 0.001 s^{-1}$			
Slip/twinning mode	$ au_0(\mathit{MPa})$	$ au_1(MPa)$	$h_0(MPa)$	$h_1(MPa)$	$h^{lphaeta}$	A_1	A_2
Basal	10	1	300	0	1		
Prismatic	78	55	450	55	1		
Pyramidal	100	150	2350	0	1		
Extension twin	35	0	0	0	1	0.65	0.75

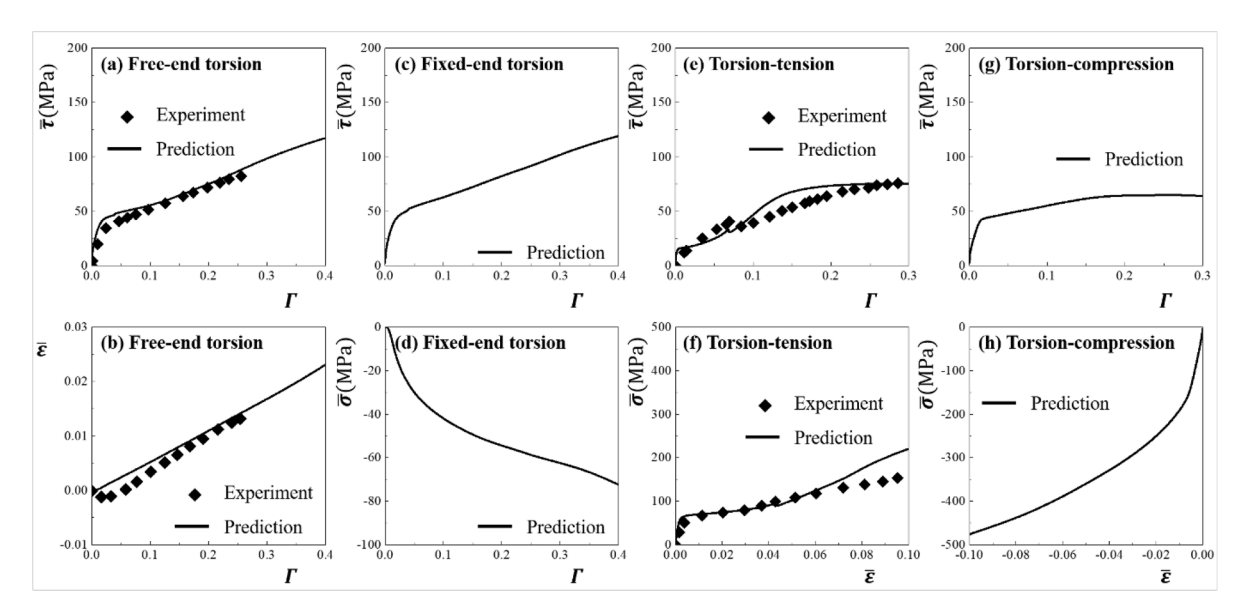


Fig. 4. (a) Average shear stress, $\bar{\tau}$, and (b) average axial strain, \bar{e} , vs. surface shear strain, Γ , of rolled-sample under free-end torsion. (c) Average shear stress, $\bar{\tau}$, and (d) average axial stress, $\bar{\sigma}$, vs. the surface shear strain, Γ , of rolled-sample under fixed-end torsion. (e) Average shear stress, $\bar{\tau}$, vs. the surface shear strain, Γ , and (f) average axial strain, \bar{e} , vs. average axial strain, \bar{e} , of rolled-sample under coupled torsion-tension. (g) Average shear stress, $\bar{\tau}$, vs. the surface shear strain, Γ , and (h) average axial strain, \bar{e} , vs. average axial strain, \bar{e} , of rolled-sample under coupled torsion-compression.

In order to avoid the solution deviating from the true equilibrium path, the equilibrium conditions (16) are added in Eq. (18). After solving (18), the increments of the sampling point stresses and the other pertinent quantities are then calculated.

Based on the EVPSC-TDT constitutive law (Section 3.1) and the equilibrium condition, the governing finite-element equations can be constructed (denoted as the TFE-EVPSC-TDT model). The coupled torsion-tension, free-end torsion, and fixed-end torsion can be simulated by the TFE-EVPSC-TDT model. Specially, the fixed-end torsion is analyzed by specifying $\dot{\lambda}=0$, while the free-end torsion by F=0. Though the resultant axial force vanishes for the free-end torsion, the axial stress is not zero and distributes over the cross-section of the rod. The results of a large strain torsion of a circular solid rod are efficiently presented in terms of the following quantities:

$$\Gamma = \frac{R_0}{L_0} \varphi, \ \overline{\tau} = \frac{3T}{2\pi R_0^3}, \ \overline{\varepsilon} = \ln\left(\frac{L}{L_0}\right), \ \overline{\sigma} = \frac{F}{\pi R_0^2}$$
 (19)

where Γ represents the shear strain at the outer surface of the cylindrical rod. $\bar{\tau}$, $\bar{\epsilon}$, and $\bar{\sigma}$ are the average shear stress, axial strain, and axial stress, respectively.

4. Results and discussion

4.1. Parameter calibration

Model parameters were calibrated by the experimentally measured stress-strain curves (Fig. 3a) under uniaxial tension and compression along the RD of the rolled AZ31 plate. The strain rate was 1.0×10^{-4} s $^{-1}$. The initial texture was discretized to 1784 orientations with corresponding different weights for the simulations. The discretized 1784 orientations were assigned to each element in the finite element model. The elastic constants (C_{ij}) (Simmons and Wang, 1971), the rate sensitivity (m), and the reference shear strain rate ($\dot{\gamma}_0$) of the Mg single crystal employed (Wang et al., 2020a) in the current work were listed in Table 1. Plastic deformation

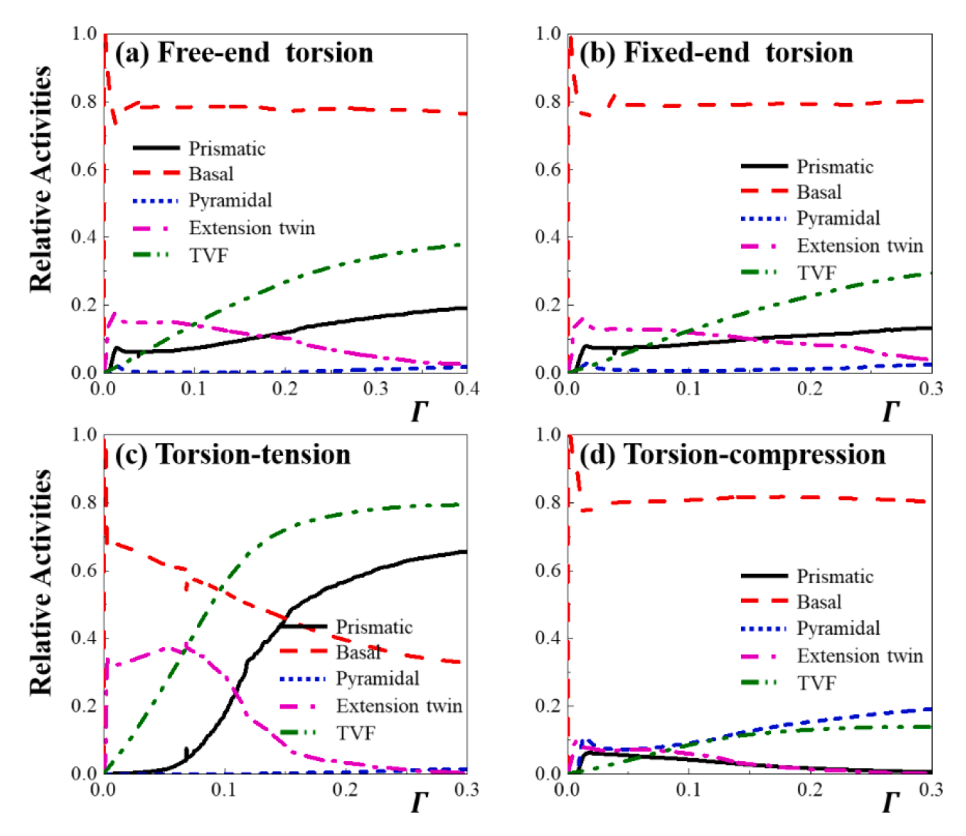


Fig. 5. The relative activities of various deformation mechanisms and the twin volume fraction at the outer surface of rolled-sample as a function of the surface shear strain in the rolled-sample under (a) free-end torsion, (b) fixed-end torsion, (c) coupled torsion-tension, and (d) coupled torsion-compression.

was assumed to be accommodated by the basal $\langle a \rangle$ slip, prismatic $\langle a \rangle$ slip, pyramidal $\langle c + a \rangle$ slip, and extension twin. The hardening parameters were determined by fitting both tensile and compressive stress-strain curves along the RD through the stand-alone EVPSC-TDT model. The calibrated hardening parameters were listed in Table 1, using which the experimental stress-strain curves were well reproduced (Fig. 3a). The calibrated parameters were applied to simulate all the deformation behaviors in response to free/fixed-end pure torsion and coupled torsion-tension/compression.

The characteristic "S" shape of the compressive stress-strain curve is attributed to massive extension twinning, while the concave-down tensile stress-strain response is mainly accommodated by the crystallographic slips, as shown in the relative activities of various deformation modes (Fig. 3b and c). The predicted twin volume fraction (TVF) under tension along the RD is relatively low (~15%, Fig. 3b). The predicted TVF under compression along the RD increases rapidly with straining and reached saturation at ~78% (Fig. 3c). This prediction has a similar trend with those experimental results documented in the literature for a similar rolled AZ31B plate deformed under compression along the RD (Carneiro et al., 2021a), as shown in the comparison in the Fig. B.2i, Appendix B. In addition, the predicted deformed textures under tension and compression (Fig. 3d) show good agreements with the measured textures (Khan et al., 2011, see the comparison in Fig. B.1a–f, Appendix B). The consistency between the simulations and the available experiments in literature demonstrates that the EVPSC-TDT model has good predictability on the evolution of texture and twinning activity.

4.2. Free-end torsion

Free-end torsions were conducted on the rolled-sample along the ND with the loading rate of $\dot{\varphi}=8.0\times10^{-4}$ rad/s before $\Gamma=0.038$, and $\dot{\varphi}=1.30\times10^{-3}$ rad/s thereafter. The measured and predicted average shear stress and average axial strain as a function of the surface shear strain for the rolled-sample were shown in Fig. 4a and b. The shear stress which yields at ~40 MPa increases with the shear strain. A significant Swift effect (Swift, 1947), i.e., the occurrence of axial strain, \bar{e} , is observed in the rolled-sample, which is owing to the anisotropic response of the material (Fig. 4b). The axial strain is extensional and increases almost linearly with the twisting for the rolled-sample. Compared with the experimental results, the shear stress response and the Swift effect of the rolled-sample under free-end torsion are well captured by the TFE-EVPSC-TDT model.

The occurrence of twinning, which is constantly evidenced in simple shear experiments (Lou et al., 2007; Kang et al., 2012), is captured by the model (Fig. 5a). The *c*-axis extension by twinning leads to a tensile axial strain in the rolled-sample with most of the

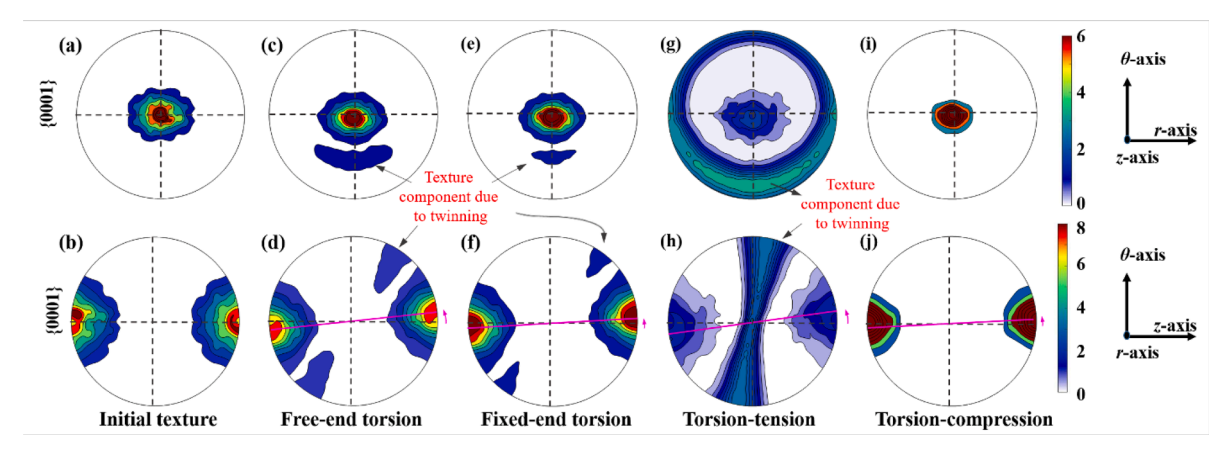


Fig. 6. The initial texture of the rolled-sample (a, b) in terms of $\{0001\}$ pole figures. The simulated results for the deformed textures characterized at the outer surface of the solid rods for the rolled-sample under (c, d) free-end torsion and (e, f) fixed-end torsion at $\Gamma = 0.4$ along with those under (g, h) coupled torsion-tension and (i, j) coupled torsion-compression at $\Gamma = 0.3$. All the textures are presented in terms of $\{0001\}$ pole figures plotted in the $\theta - r$ plane and $\theta - z$ plane, respectively.

basal poles oriented along the z-axis. Obviously, the basal slip system dominates the entire deformation during the free-end torsion (taking \sim 80% of the total activities); however, the roles of pyramidal slips are trivial. Compared with the dominant roles of basal slips, the prismatic slip and extension twin are relatively less active (taking up to \sim 20% of the total activities). The twin volume fraction (TVF) at the outer surface increases with the shear strain, attaining 38% at Γ =0.4 under the free-end torsion of the AZ31 Mg alloy rod. Although the TVFs were not measured in our materials, the predicted TVFs at the outer surface show a similar increasing trend with the measured TVFs under free-end torsion of the AZ31 tube in Carneiro et al. (2021) (Fig. B.1g, Appendix B).

The simulated results for the deformed textures at the outer surface of the rolled-sample at $\Gamma=0.4$ are plotted in the Fig. 6c and d. As displayed in the $\{0001\}$ pole figure represented in the $\theta-r$ plane (Fig. 6c), a texture component is developed in the region away from the center along the negative direction of the θ -axis. This texture component is attributed to the extension twins developed during free-end torsion (Carneiro et al., 2021b). Such a twinning texture component could also be observed in the $\theta-z$ plane, where a small part of the basal pole rotates about the r-axis by \sim 45 along the circumstance of the pole figure from the z-axis toward the θ -axis. In addition, a typical shear texture component caused by crystal rotation due to shear deformation of the matrix grains is visible in the $\theta-z$ plane, i.e. that the basal poles of the matrix grains are rotated by \sim 5° about the r-axis in the $\theta-z$ plane. The predicted deformed texture of the rolled-sample at the outer surface under free-end torsion is consistent with the trend of the measured texture in the AZ31 tube under free-end torsion (Carneiro et al., 2021a) (see the comparison in Fig. B.2c and f, Appendix B).

As we know, the main difference between simple shear and pure torsion is the inhomogeneity of the internal stress/strain within the rods. By means of our TFE-EVPSC-TDT model, the multiaxial inhomogeneity can be clearly visualized by the distribution of the stress components along the normalized radius direction (r/R_0) in the solid rods under free-end torsion at shear strains $\Gamma=0.2$ (Fig. 7a) and $\Gamma=0.4$ (Fig. 7b). Obviously, the solid rod is subjected to multiaxial stress, and all the stress components distribute nonlinearly along the radius. The stress components distribute in a similar fashion at the two shear strain levels only with a quantitative difference. Specifically, the stress component, σ_{zz} , varies from compressive to tensile for the rolled-sample at $\Gamma=0.2$ and 0.4 to meet the requirement of zero resultant axial force under the free-end torsion loading.

4.3. Fixed-end torsion

Fig. 4c and d showed the simulated torsional responses of the rolled-sample under fixed-end torsion. The corresponding experimental results were not available. For numerical simulations, the applied twisting rates of the fixed-end torsions were prescribed the same as those for the free-end torsion. Compared with the free-end torsion, the only difference for the fixed-end torsion lay in the boundary condition, where the axial displacement/strain at the end surface was constrained ($\bar{\epsilon} = 0$). As presented in Fig. 4d, the average axial stress is compressive and its absolute value increases with the twisting for the rolled-sample under the fixed-end torsion. The trends of the shear stress response under the fixed-end torsion (Fig. 4c), along with the corresponding relative activities of deformation mechanisms (Fig. 5b) and the deformation textures (Fig. 6e and f), are similar to what are obtained under the free-end torsion, respectively.

The distribution of the stress component, σ_{zz} , is different from that under the free-end torsion (Fig. 7c and d). The total axial force, i. e. the integration of the axial stress along the radius, is not necessarily zero because the axial strain, \bar{e} , is fixed at zero for the fixed-end torsion. The stress component, σ_{zz} , is compressive along the radius for the rolled-sample at $\Gamma=0.2$ and 0.4. The stress components, σ_{rr} and $\sigma_{\theta\theta}$, distribute almost linearly along the radius.

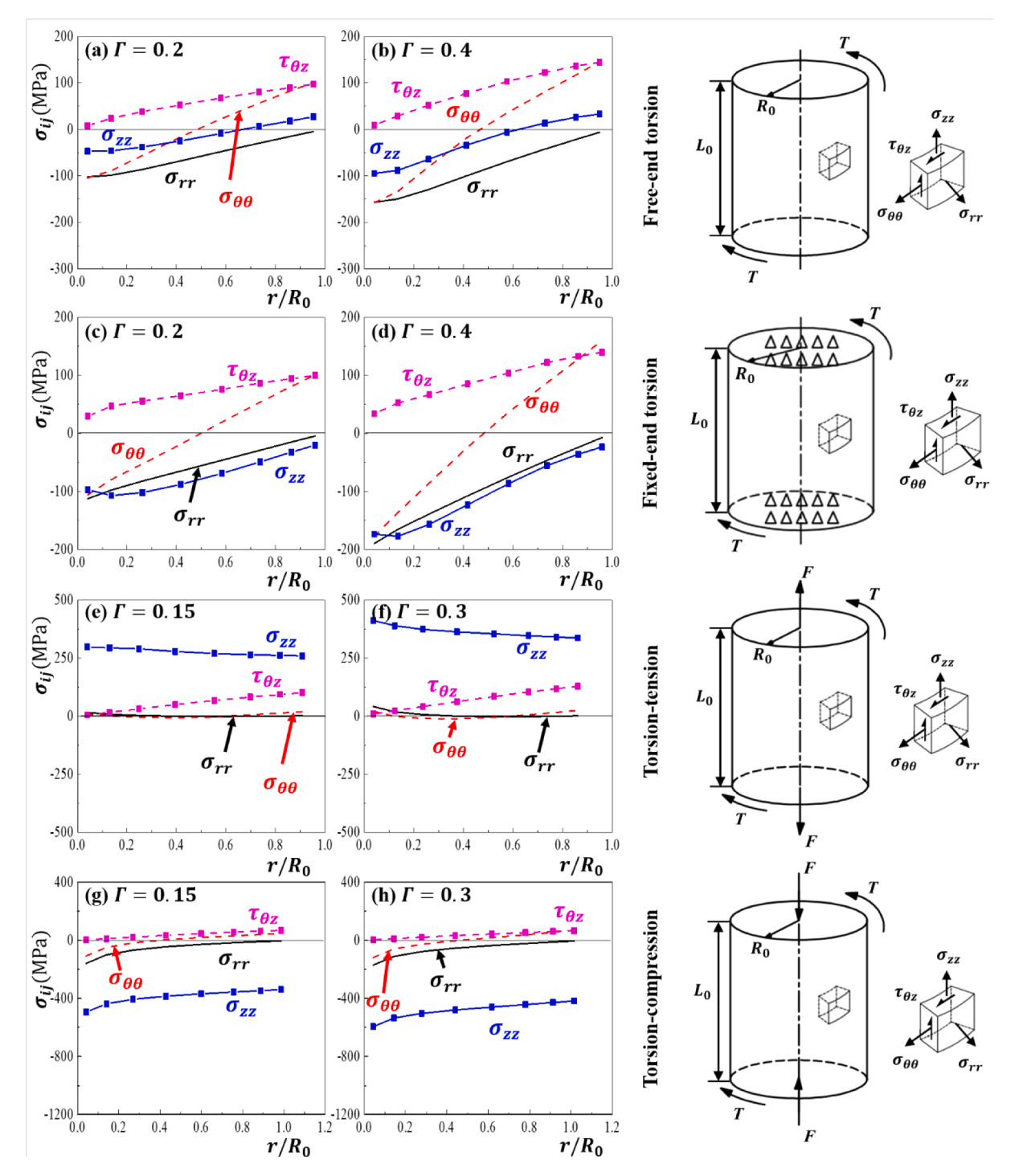


Fig. 7. Distribution of the stress components as a function of normalized radius (r/R_0) in the solid rods for the rolled-sample under (a, b) free-end torsion at $\Gamma=0.2$ and 0.4, (c, d) fixed-end torsion at $\Gamma=0.15$ and 0.3, and (g, h) coupled torsion-compression at $\Gamma=0.15$ and 0.3.

4.4. Coupled torsion-tension

The coupled torsion-tension tests had been conducted for the rolled-sample. The loading rates were taken as $\dot{\varphi}=1.9\times10^{-2} {\rm rad/s}$ and $\dot{\bar{\varepsilon}}=3.0\times10^{-3}\,{\rm s}^{-1}$ before $\Gamma=0.068$, and $\dot{\varphi}=2.1\times10^{-3}{\rm rad/s}$ and $\dot{\bar{\varepsilon}}=4.0\times10^{-4}\,{\rm s}^{-1}$ thereafter. Compared with the pure torsional behaviors (Fig. 4a–d), both the average shear stress-strain curve (Fig. 4e) and the average axial stress-strain curve (Fig. 4f) of

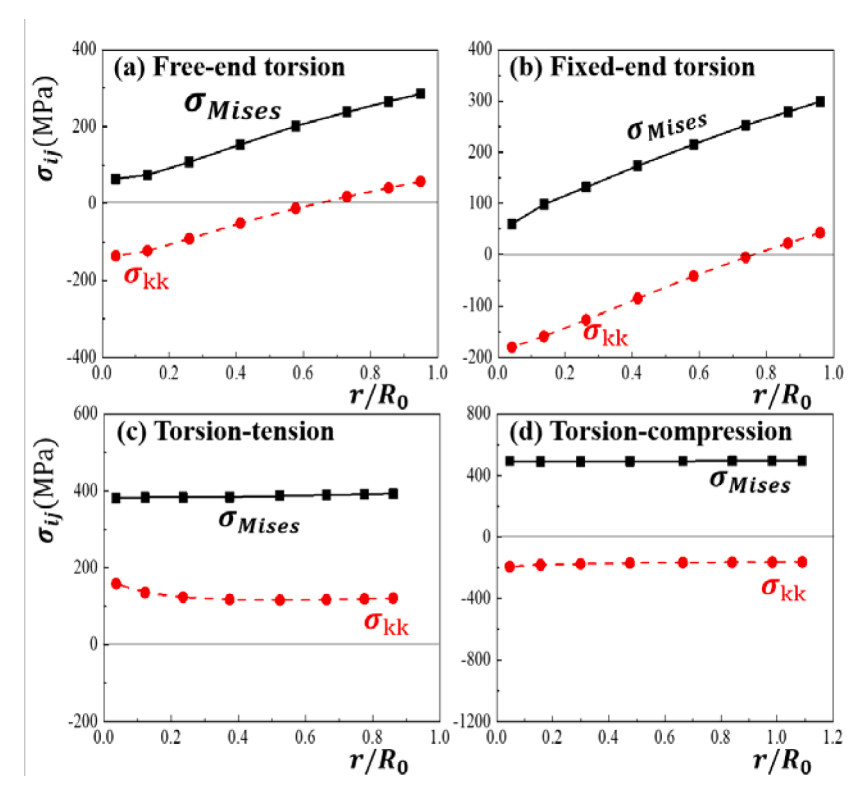


Fig. 8. Distributions of the von-Mises stress and the bulk stress along the radius in rolled-sample under (a) free-end torsion, (b) fixed-end torsion at a shear strain of $\Gamma = 0.4$ and under (c) coupled torsion-tension and (d) coupled torsion-compression at a shear strain of $\Gamma = 0.3$.

the rolled-sample under the coupled torsion-tension exhibit a characteristic "S" shape. This is attributed to the increased twinning activities induced by the coupling of torsion and tension (Fig. 5c). The S-shape in both shear and axial stress-strain responses is not so obvious as that of the stress-strain curve under uniaxial compression (Fig. 3a). This is because twinning under torsion-tension is less active (Fig. 5c) than that of uniaxial compression (Fig. 3c).

Due to the coupling of axial and torsional loadings, the activities of the deformation mechanisms change greatly. Specially, the activity of extension twinning in the torsion-tension deformation ($\Gamma < 0.1$) is almost twice as those operated in the free-end or fixed-end torsion (compare Fig. 5c to . 5a and b). As seen in Fig. 5c, the basal slip persistently plays a dominant role under torsion-tension, whereas the pyramidal slip is rarely active. The contribution of prismatic slip becomes significant with the increasing shear strain. At $\Gamma = 0.3$, the activity of prismatic slip reaches as high as \sim 65% (Fig. 5c). In parallel, the TVF evolves to \sim 80% at $\Gamma = 0.3$ at the outer surface of the rolled-sample under coupled torsion-tension. This result implies that twinning may be tunable by combining different magnitudes of axial loading and torsional loading.

The deformed textures under the coupled torsion-tension at $\Gamma=0.3$ in terms of the $\{0001\}$ pole figures were shown in Fig. 6g and h. Similar to the pure torsion, the shear texture component is also observed in the $\{0001\}$ pole figures where the basal poles of the matrix grains are rotated by $\sim 5^\circ$ about the r-axis in the $\theta-z$ plane. Additionally, the texture component due to twinning is visualized by part of the basal pole rotating about the r-axis by $\sim 80^\circ$ in the $\theta-z$ plane. This strong twin texture component indicates that profuse twinning is undergoing in the rolled-sample under torsion-tension, which is confirmed by the nearly 80% TVF at $\Gamma=0.3$ (Fig. 5c).

Similar to the pure torsion, a multiaxial stress state exists in the rolled-sample under coupled torsion-tension and all the stress components distribute nonlinearly along the radius (Fig. 7e and f). The normal stress components, σ_{zz} , are all in tension, but interestingly, their magnitudes are higher near the center than those near the outer radius. This trend is ascribed to the interaction between the neighboring elements, *i.e.* different cylindrical layers. Under the coupled torsion-tension, more twins are generated by the higher magnitudes of the shear stress components near the outer radius, thus inducing a higher extension along the z-axis near the outer radius than that near the inner radius. To balance such a difference in extension between the inner and outer radii, higher magnitudes of the normal stress components σ_{zz} are resulted near the center than those near the outer radius of the rods.

4.5. Coupled torsion-compression

As the experimental results were not available for the rolled-sample along the ND under the coupled torsion-compression, only the simulated mechanical responses were presented in Fig. 4g and h. The applied twisting rate and the axial strain rate in simulations are $\dot{\varphi} = 4.0 \times 10^{-2}$ rad/s and $\dot{\bar{\epsilon}} = -3.9 \times 10^{-3}$ s⁻¹, respectively. As shown in Fig. 4g and h, both the average shear stress-strain response

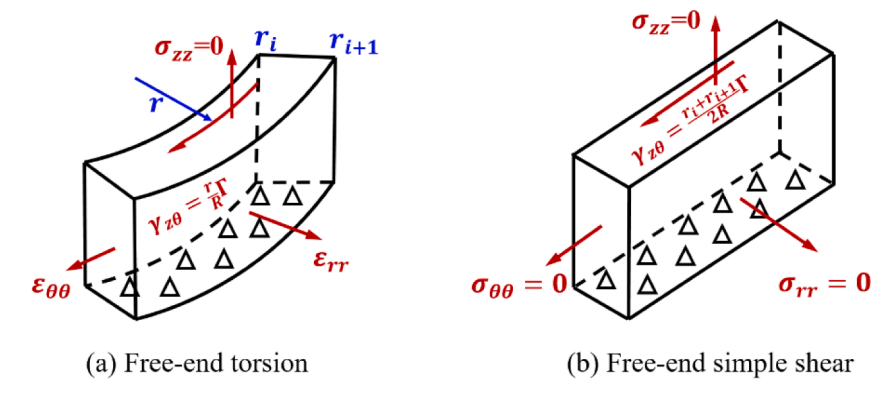


Fig. 9. The boundary conditions for the free-end torsion along with the analogous simulation for the free-end simple shear.

and the average axial stress-strain response of the rolled-sample have a concave-down shape, which is different from the "S" shape exhibited in those under the coupled torsion-tension (Fig. 4e and f). Such a difference is rooted in the fact that extension twinning is suppressed under the coupled torsion-compression. As evidenced in Fig. 5d, the relative activity of twinning takes less than 10% when $\Gamma < 0.1$.

As seen in Fig. 5d, the contribution of the basal slips takes the highest fraction out of all the deformation mechanisms under the coupled torsion-compression. Specially, the pyramidal slips are activated and operated under the coupled torsion-compression, mainly ascribed to the fact that the CRSS of the pyramidal slip is exceeded due to the coupled axial compression. With the increasing of the shear strain, the fraction of the pyramidal slip activity increases and reaches \sim 20% when $\Gamma > \sim 0.15$. The TVF under the coupled torsion-compression is much lower than those under the pure torsion and coupled torsion-compression, and achieves only \sim 15% at $\Gamma = 0.3$, which confirms that twinning is suppressed by the coupled axial compression.

The coupled torsion-compression strengthened the initial basal texture as shown in the deformed texture of the rolled-sample at $\Gamma=0.3$ (Fig. 6i and j). The shear texture component is visible in the {0001} pole figures with the basal poles of the matrix grains rotated by $\sim 2^{\circ}$ about the *r*-axis in the $\theta-z$ plane. Different from the pure torsion and the coupled torsion-tension, the twin texture component is invisible in the {0001} pole figures. This is likely associated with the suppression of twinning under the coupled axial compression loading. As an additional deformation feature in response to the coupled axial compression, the stress components σ_{zz} are all compressive with their magnitudes being much higher than those of the other stress components including $\sigma_{\theta\theta}$, σ_{rr} and $\tau_{\theta z}$ (Fig. 7g and h).

5. Further discussion

5.1. Multiaxial inhomogeneity in torsional behaviors

Compared with the simple shear, a unique feature of the torsion experiments (including the free/fixed-end torsion and the coupled torsion-tension/compression) is the presence of internal deformation in a multiaxial stress state which distributes inhomogeneously along the radius within the solid rod. Such a multiaxial inhomogeneity could be clearly visualized by the distribution of stress components (Fig. 7) and further confirmed by the spatial distribution of the invariants of the stress tensor at the inner elements of the solid torsion rod. Fig. 8 presents the distributions of the von Mises stress σ_{Mises} and the bulk stress $\sigma_{\text{Kk}} = (\sigma_{rr} + \sigma_{\theta\theta} + \sigma_{zz})/3$ along the radius in the rolled-sample under the free-/fixed-end torsion at $\Gamma = 0.4$ and under the coupled torsion-tension/compression at $\Gamma = 0.3$. An increasing trend of the von Mises stress with the increasing radius is shown under pure torsion, yet such a trend is much diminished under the coupled torsion-tension/compression. The distributions of the bulk stress under pure torsion reveal that the inner elements are compressed while the outer elements are stretched due to the mutual interaction between elements. Regarding the coupled torsion-tension/compression, the bulk stresses are positive and negative, respectively. That is corresponding to the predominant tensile and compressive stress components σ_{zz} . Specially, the bulk stress under the coupled torsion-tension is larger at the inner radius, which is a result of the strong mutual interaction among the elements. In short, the multiaxial inhomogeneity is present in all the torsional behaviors, regardless of pure torsion or coupled torsion-tension/compression.

5.2. Comparison between pure torsion and simple shear

As discussed in the introduction, simple shear and pure torsion are two common tests to characterize the shear response of materials. Comparatively, the torsion test has been employed more often than the simple shear test because the latter is difficult to sustain a homogenous shear deformation at a large strain. We have demonstrated in Fig. 8 that the interaction between the internal elements is strong under the torsion of the solid rod. This feature leads to an interesting question: what is the difference between these two types of shear tests?

To demonstrate the difference, free-end simple shear and fixed-end simple shear were simulated using the initial texture of the

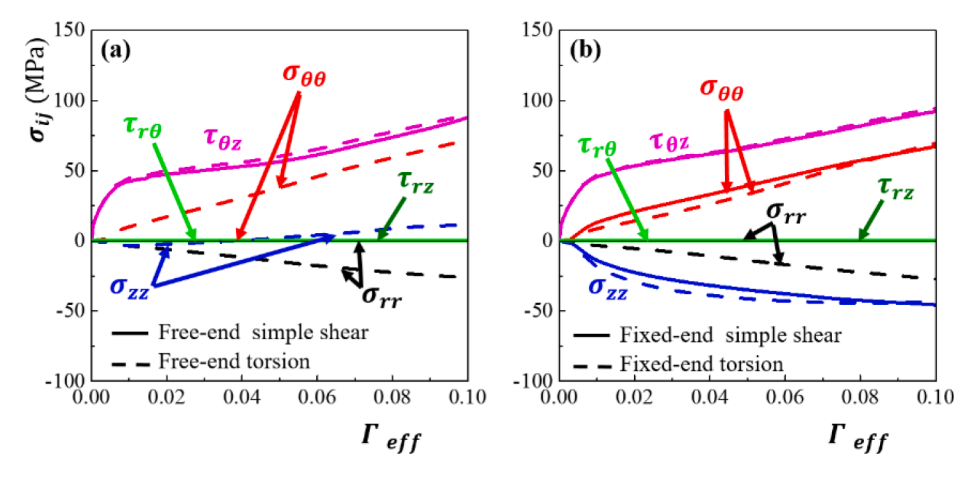


Fig. 10. The stress components as a function of the shear strain in the element at $r/R_0 = 0.67$ under (a) the free-end torsion, and (b) the fixed-end torsion along with their analogous simulations for the simple shear.

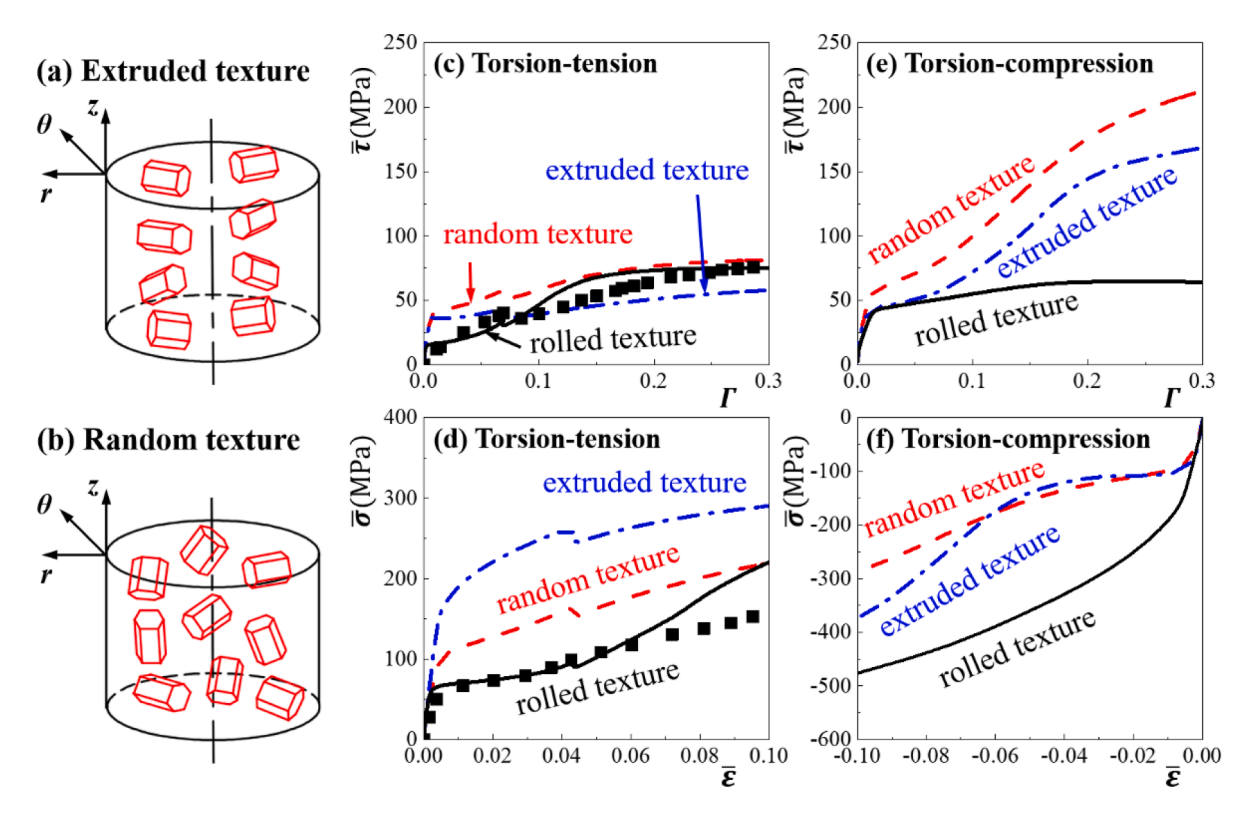


Fig. 11. The schematic of the initial (a) extruded texture and (b) random texture. Average shear stress, $\bar{\tau}$, as a function of the surface shear strain, Γ , in the specimens with three initial textures under (c) coupled torsion-tension and (e) coupled torsion-compression. Average axial stress, $\bar{\sigma}$, as a function of average axial strain, $\bar{\epsilon}$, of three initial textures under (d) coupled torsion-tension and (f) coupled torsion-compression.

rolled-sample. The boundary conditions (BCs) of these simulations were set to be basically the same as a thin cylindrical element of the solid rod (here, the element at $r=0.67R_0$ was taken). Specifically, the BCs for the free-end simple shear were: $\dot{\gamma}_{\theta z}=0.67\dot{\Gamma}$, with all the other normal stress components set to be zero. The different BCs for the element under free-end torsion and free-end simple shear were illustrated in Fig. 9, where the ε_{rr} and $\varepsilon_{\theta\theta}$ in Fig. 9a are informed from the interaction between adjacent elements by the TFE-EVPSC-TDT model. For the cases of the fixed-end simple shear, $\dot{\gamma}_{\theta z}=0.67\dot{\Gamma}$ remained the same as that in the free-end simple shear but $\sigma_{zz}=0$ is changed to $\varepsilon_{zz}=0$. As $\gamma_{\theta z}=\frac{r}{R_0}\Gamma=\frac{r}{L_0}\varphi$, the shear strain component $\gamma_{\theta z}$ distributes linearly across the thickness. Since the embedded cylindrical element is thin, this inhomogeneity is small and could be ignored in the corresponding analogous simulations.

The two sets of simulation results are compared in Fig. 10. The primary shear stress components show almost the same responses for

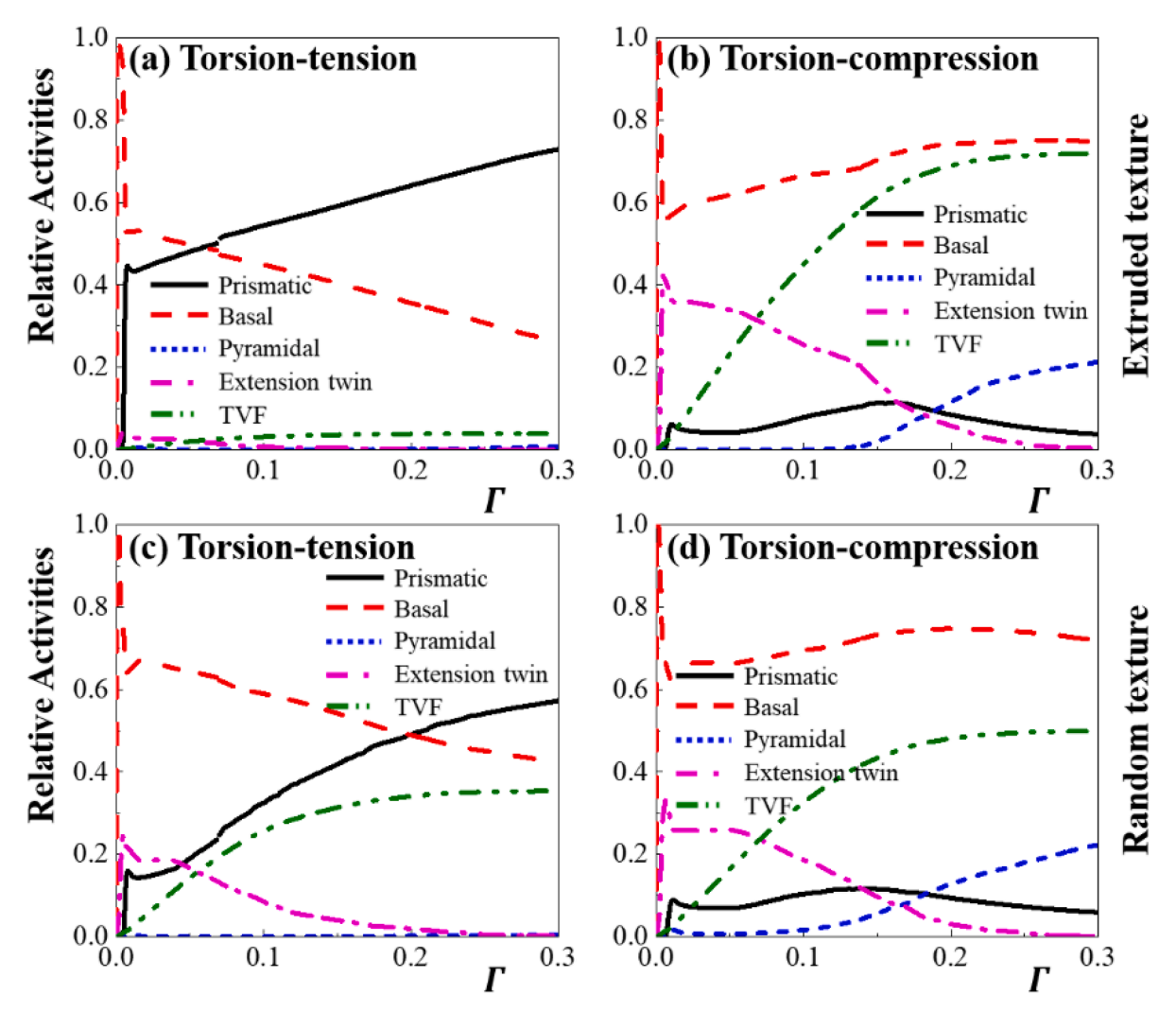


Fig. 12. The relative activities of various deformation mechanisms and the volume fraction of the extension twin at the outer radius of the specimens with (a, b) extruded texture and (c, d) random texture under coupled torsion-tension and coupled torsion-compression.

both the pure torsion and the analogous simple shear. However, there are great differences in the normal stress components between the two cases. Apparently, the difference arises from the ignored inhomogeneity of the shear strain component and the constraints from the adjacent elements, which confirms that the significant bulk stress occurs within the solid rod (Neale et al., 1990). The difference in the normal-stress components between the analogous simple shear and the pure torsion highlights the importance of accounting for the inhomogeneity in a torsion test as the stress states are inherently in a multiaxial state which activates the operation of different deformation mechanisms.

5.3. Initial texture effects on the coupled torsion-tension/compression behavior

Numerous studies had shown that the initial texture had a significant effect on the mechanical responses of magnesium alloys. To explore such texture effects on the coupled torsion-tension/compression behavior of Mg alloy solid bar, we have carried out further simulations using the TFE-EVPSC-TDT model with two additional axisymmetric initial textures, *i.e.*, extruded texture (Fig. 11a) and random texture (Fig. 11b). The extruded texture was constructed resembling a typical extruded texture similar to that from Agnew et al. (2006) and axial direction (z) aligns along the extrusion direction (Fig. 11a). The hardening parameters of the simulations for the extruded and random textures were taken the same as those used for the rolled-sample (Table 1, and the rolled-sample was denoted as the rolled texture for consistency). For simulations under torsion-tension/compression loading paths, the twist rate and the axial strain rate were prescribed the same for the random and extruded textures as those for the rolled texture.

The stress-strain responses for the samples with different initial textures (Fig. 11c-f) clearly displayed a strong texture dependency. Specifically, under the coupled torsion-tension (Fig. 11c and d), the yield shear stress of the specimen with random texture was the highest, while that of the specimen with rolled texture was the lowest. In contrast, the axial yield stress of the specimen with extruded

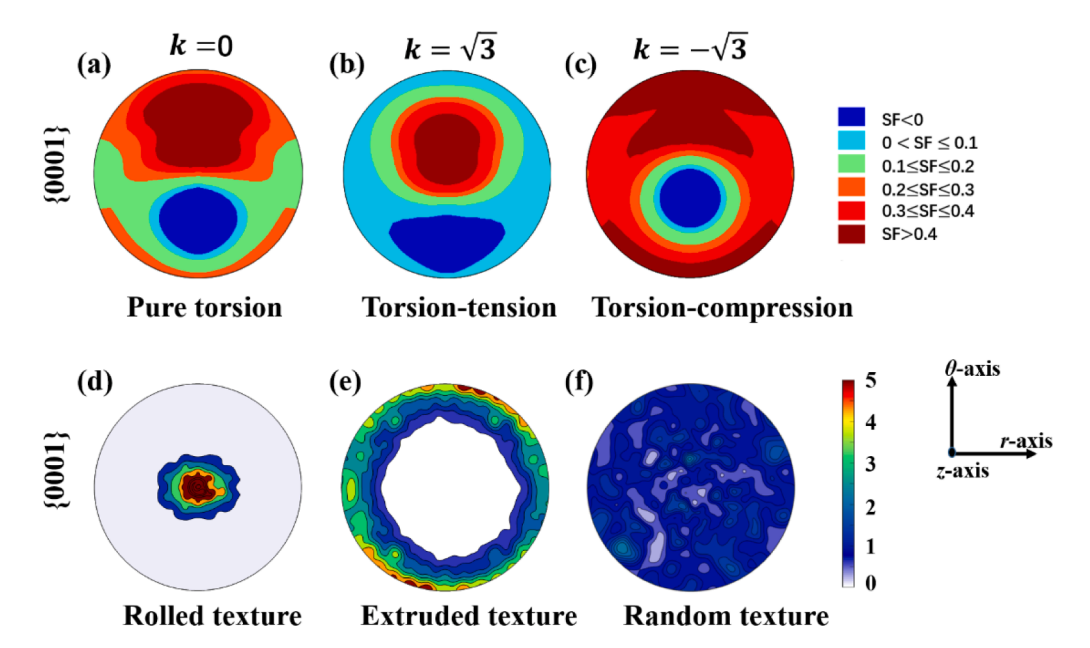


Fig. 13. Twinning Schmidt factor {0001} pole figures under the loadings of (a) free/fixed-end torsion (k = 0), (b) torsion-tension (k > 0), (c) and torsion-compression (k < 0). The {0001} pole figures plotted in the $\theta - r$ plane for the specimens with (d) rolled texture, (e) extruded texture, and (f) random texture, respectively.

texture was higher than those of the specimens with the other two textures. An S-shape was observed in both the shear and axial stress-strain responses in the specimen with rolled texture, yet such an S-shape was invisible in the specimens with extruded and random textures. The presence and absence of the S-shape in the stress-strain responses were ascribed to the promotion and suppression of the extension twinning in the specimens with different textures under coupled torsion-tension.

Under coupled torsion-compression, both the average shear and axial stress-strain responses in the specimens with extruded and random textures exhibited the S-shape, which was different from the concave shape of the stress-strain responses in the specimen with rolled texture (Fig. 11e and f). The cause of such a difference was ascribed to the fact that extension twinning was suppressed in the specimen with rolled texture but promoted or partially promoted in the specimen with extruded texture or random texture under coupled torsion-compression.

Fig. 12 shows the relative activities of various deformation mechanisms and the corresponding twin volume fraction at the outer radius of the specimens with extruded texture and random texture under different loadings. As for the coupled torsion-tension loading path (Fig. 12a and c), the basal slip and the prismatic slip accommodate the plastic deformation in specimens with both the extruded texture and the random texture wherein the pyramidal slips are rarely active. For the specimens with extruded and random textures under torsion-compression (Fig. 12b and d), the basal slip dominates the deformation while the contribution of prismatic slip is relatively less. The pyramidal slip takes place when the shear strain increases over 15%.

As we know, the extension twin can be activated if a grain is under tension along the c-axis or under compression perpendicular to the c-axis. The c-axes of most grains in the specimen with extruded texture are perpendicular to the axial direction. Therefore, the extension twin is suppressed by the axial tensile stress and promoted by the axial compressive stress in the specimen with extruded texture (Fig. 12a and b). Because of the random distribution of grain orientations in the specimen with random texture, both loading conditions have equivalent favorability for twinning. Therefore, the extension twin is relatively active under either torsion-tension or torsion-compression (Fig. 12c and d). In line with the twinning activity, the twin volume fraction (TVF) evolves to \sim 80% and \sim 15% at the outer radius of the specimen with rolled texture at $\Gamma=0.3$ under the coupled torsion-tension and torsion-compression, respectively, while the TVF evolves to \sim 5% and 70% in the specimen with extruded texture and \sim 35% and \sim 50% in the specimen with random texture. The difference in the TVFs suggests that twinning is tunable through coupling axial and torsional loadings with different initial textures.

5.4. Twinning within the rods

In *hcp* materials, mechanical twinning plays an important role in the deformation of materials. To discuss the twinning activity within the solid torsion rod, the twinning favorability is analyzed in terms of a modified twinning Schmid factor (SF). Because of the multiaxial stress state, the SF is calculated as the ratio of the resolved shear stress (RSS) on a twin plane to the von Mises stress under a specific loading condition. As only the dominant stress components are considered, the stress states under different loadings are given as below:

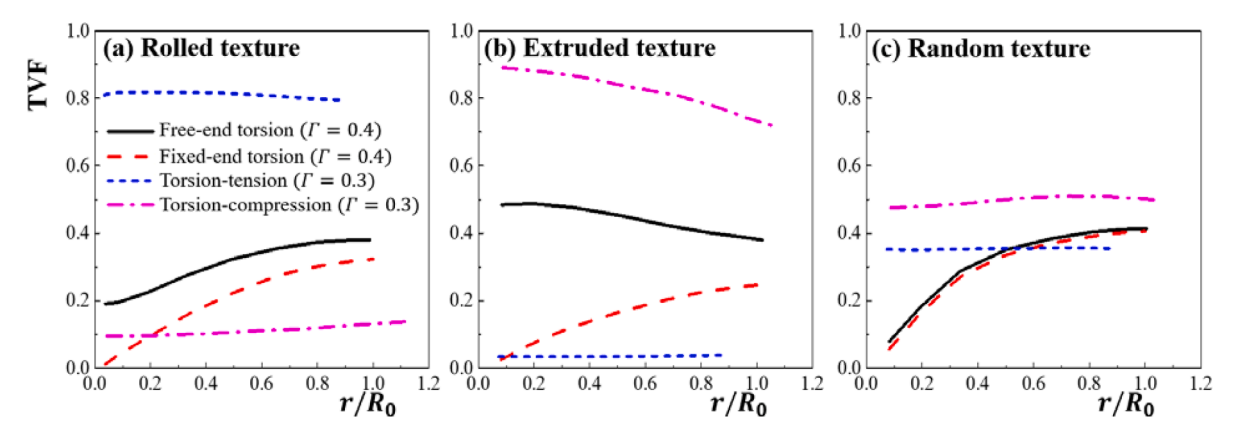


Fig. 14. Distribution of the TVFs along the radius under four different loadings in specimens with the (a) rolled texture, (b) extruded texture, and (c) random texture.

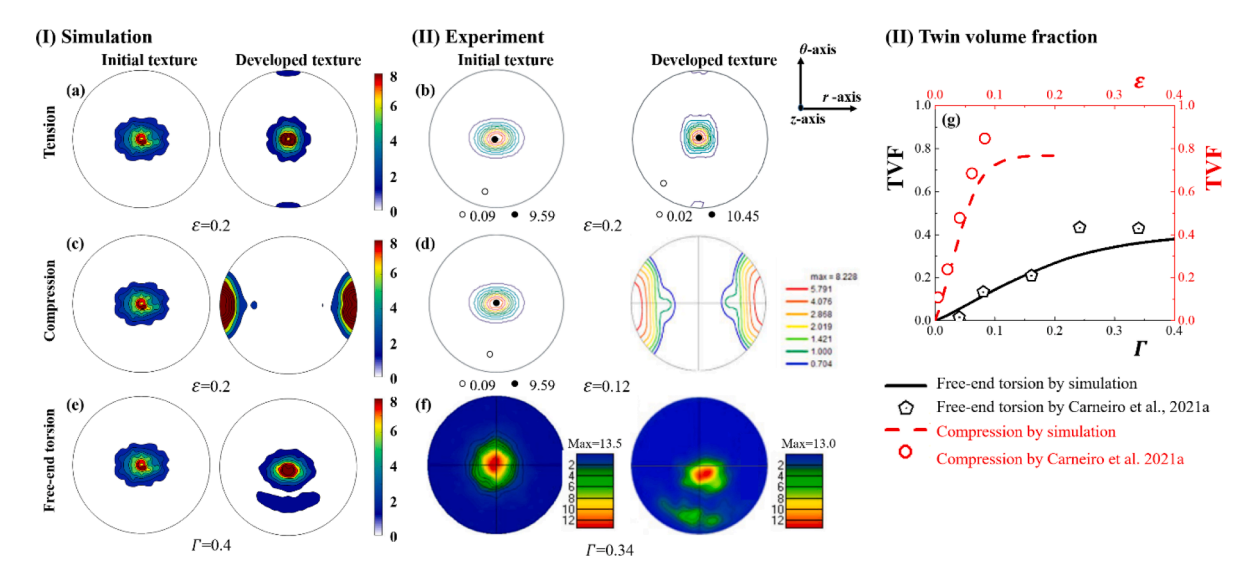


Fig. 15. Simulated and experimental deformation textures in terms of {0001} pole figures of AZ31 Mg alloy under (a, b) tension, (c, d) compress and (e, f) free-end torsion, where the experimental textures were taken from Khan et al. (2011) for AZ31 sheet under tension and compression and Carneiro et al. (2021a) for AZ31 tube under free-end torsion. (g) Predicted and experimental twin volume fractions (TVFs) as a function of the axial strain (ε) under compression and the shear strain (Γ) under free-end torsion, where the experimental TVFs were taken from Carneiro et al. (2021a).

$$\sigma_{ij} = \begin{bmatrix} \sigma_{rr} & \sigma_{r\theta} & \sigma_{rz} \\ \sigma_{\theta r} & \sigma_{\theta \theta} & \sigma_{\theta z} \\ \sigma_{zr} & \sigma_{z\theta} & \sigma_{zz} \end{bmatrix} = \begin{bmatrix} 0 & 0 & 0 \\ 0 & 0 & \tau \\ 0 & \tau & k\tau \end{bmatrix}$$

$$(20)$$

where τ is the primary shear stress, $k\tau$ is the primary normal stress component. Different loadings can be simulated by adjusting k, i.e., k=0 for free/fixed-end torsions, k>0 for coupled torsion-tension, and k<0 for coupled torsion-compression. The von Mises stress is $\sigma_e=\tau\sqrt{k^2+3}$, and the theoretical range of the SF is $[-1/\sqrt{3},1/\sqrt{3}]$. The twinning SF of grain orientation is selected as the largest one among the six twinning variants. To better illustrate the orientation dependency of the twinning favorability, the twining SFs are plotted in the {0001} pole figures associated with different loadings (see Fig. 13). The grain orientations where the twinning SFs falling into the orange, red and brown areas (SF > 0.2) are favorable for twinning. In contrast, the grain orientations projected to the blue area (SF < 0) are not favorable for twinning.

For the rolled texture, the pole figure shows a strong basal texture. The SFs for extension twinning are higher near the center of the (0001) pole figure under coupled torsion-tensions (k > 0) (Fig. 13b), the extension twin is more favored, as confirmed by the simulation (Fig. 5c). However, the twinning SFs are small and even negative near the center of the pole figure under coupled torsion-compression (k < 0) (Fig. 13c), the extension twinning is unfavorable in the rolled texture as confirmed in Fig. 5d. Under pure torsion (k = 0), the rolled texture has comparable amounts of grains falling into the twinning favorable areas (Fig. 13a), so the developed TVFs are similar to each other for free-end and fixed-end torsion (Fig. 5a,b). For the extruded texture (Fig. 13e), the pole figure shows a

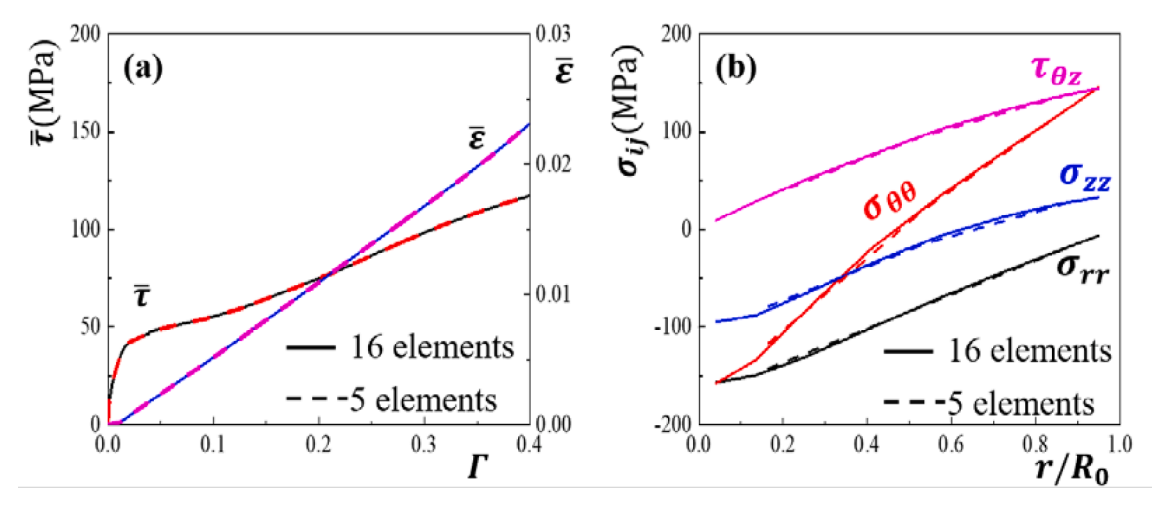


Fig. 16. Mesh-sensitivity study: (a) Average shear stress, $\bar{\tau}$, and axial strain, $\bar{\epsilon}$, as a function of the surface shear strain, Γ, of rolled-samples under free-end torsion with meshing using 16 and 5 elements. (b) The corresponding distribution of stress components as a function of normalized radius (r/R_0) in the solid rod at surface shear strain $\Gamma = 0.4$.

strong basal texture with most of the c-axes oriented perpendicular to the z axis. Therefore, the twinning favorability under different loadings in the extruded texture is regarded almost the opposite to those in the rolled texture. Specifically, the extension twinning in the specimen with extruded texture is favorable under torsion-compression but unfavorable under the torsion-tension. As for the random texture (Fig. 13f), the twinning favorability is almost equivalent in all three loading paths.

The inhomogeneity nature of the torsional deformation of the Mg alloy solid bar makes the twinning activity strongly dependent on the local stress state that distributes heterogeneously along the radial direction. The distributions of the developed TVFs in the specimens with three initial textures at specific surface shear strains under four loading conditions are presented in Fig. 14. Under either free-end torsion or fixed-end torsion, the TVFs in specimens with the rolled texture and random texture increase when the radius increases from the center to the outer surface of the rod. The TVFs in the specimen with extruded texture under free-end torsion increase with the radius, whereas those under fixed-end torsion show a slightly decreasing trend. In addition, the TVFs in specimens with three textures under fixed-end torsion are slightly less than those under free-end torsion. In other words, the constraint, $\bar{\epsilon} = 0$, of the fixed-end torsion, inhibits the twinning activity to some extent in all three textures. The difference of the TVFs between the free-end torsion and fixed-end torsion is not large in specimens with rolled and random textures, while such difference is relatively large in specimen with extruded texture. This is likely originated from the fact that the fraction of twinning-favorable grains in specimen with extruded texture is higher than that in specimens with rolled and random textures under these two pure torsion conditions (Fig. 13).

Regarding the coupled torsion-tension/compression loading conditions, the effect of the initial texture on the distribution of TVFs is pronounced. For the specimen with rolled texture (Fig. 14a), significant twinning up to $\sim\!80\%$ TVF is present at $\Gamma=0.3$ under the coupled torsion-tension, while the TVF under torsion-compression takes only up to $\sim\!12\%$. The TVF in specimen with extruded texture (Fig. 14b) under torsion-tension is the least, reaching $\sim\!4\%$ at $\Gamma=0.3$, whereas the TVF under torsion-compression takes up to $\sim\!75\%$. For the specimen with random texture (Fig. 14c), the TVF under torsion-tension is up to $\sim\!35\%$, and the TVF under torsion-compression reaches $\sim\!50\%$ at $\Gamma=0.3$. Interestingly, the TVFs in the specimen with extruded texture under coupled torsion-tension and free-end torsion display a subtle decreasing with the increase of the radius. The TVFs in specimens with rolled texture and random texture under coupled torsion-tension/compression remain nearly constant throughout the radius.

Nevertheless, it is revealed that the twinning activity is drastically affected by the axial stress state rather than the shear stress, which either suppresses or promotes twinning in different initial textures. Furthermore, the results in Fig. 14 indicate that a gradient distribution of twins could be designed and tuned in bulk Mg alloy solid bar by coupling torsion and tension/compression with different textures. Stepping further, it is thought that our torsion-specific crystal plasticity model may provide a novel design tool for fabricating bulk Mg alloys with tunable pre-twinned structures that may carry optimized mechanical properties (Hong et al., 2010; Culbertson et al., 2017; Song et al., 2017).

6. Conclusions

The torsional and coupled torsion-tension/compression behaviors of an AZ31 Mg alloy rolled sample were investigated both experimentally and numerically. In addition, texture effects (rolled, extruded, and random) on the coupled torsion-tension/compression behaviors were investigated numerically. Based on the results, the following conclusions could be drawn:

(1) The free-end torsion and coupled torsion-tension tests have been conducted on the solid rod having an initial rolled basal texture. The EVPSC-TDT crystal-plasticity model, in conjunction with the torsion-specific finite-element approach, was employed to simulate pure torsions and torsion-tension/compression for the sample with rolled texture.

- (2) The anisotropic and inhomogeneous nature of the mechanical responses in the Mg alloy solid rod under torsional loading is successfully captured. The operating deformation mechanisms alter significantly under various torsional loadings. The basal slip system dominates the entire deformation under the free-/fixed-end torsion, the extension twinning is promoted under torsion-tension, while is suppressed under torsion-compression.
- (3) The Swift effect, where axial strain is extensional in the specimen with rolled texture under free-end torsion, is well captured by the model. Regarding the fixed-end torsion, a compressive axial stress for the specimen with rolled texture is predicted by the model as well.
- (4) Due to the difference in the stress state, different deformation textures are developed after loading under free- or fixed-end torsion and coupled torsion-tension/compression paths. The predicted deformation textures are consistent with those shear textures available in the literature.
- (5) Deformation twinning is nearly equally active in specimens with three different textures (rolled, extruded, and random) under either free-end torsion or fixed torsion. However, the coupled axial stress would affect the twinning activities drastically. Twinning is suppressed by the coupled axial tension in the specimen with extruded texture, while it is promoted in the specimen with rolled texture. In contrast, twinning is promoted by the coupled axial compression in the specimen with extruded texture but suppressed in specimen with the rolled texture.
- (6) The multiaxial inhomogeneity is present in all the torsional loading paths, regardless of pure torsion or coupled torsion-tension/compression. The analogous simulation comparison between the simple shear and pure torsion confirms that a significant bulk stress occurring within the solid rod is attributed to the strong interaction between the cylindrical elements under torsional loadings.

CRediT authorship contribution statement

Huamiao Wang: Conceptualization, Methodology, Software, Funding acquisition, Writing – review & editing. **Xiaodan Zhang:** Investigation, Data curation, Conceptualization, Writing – original draft, Writing – review & editing. **Wei Wu:** Investigation, Writing – review & editing. **Peter K. Liaw:** Resources, Writing – review & editing. **Ke An:** Investigation, Writing – review & editing. **Qin Yu:** Conceptualization, Methodology, Supervision, Writing – review & editing. **Peidong Wu:** Supervision, Writing – review & editing.

Declaration of Competing Interest

The authors declare that they have no known competing financial interests or personal relationships that could have appeared to influence the work reported in this paper.

Acknowledgment

HW was supported by the 2020-JCJQ project (GFJQ2126-007), the National Natural Science Foundation of China (Nos. 51975365 and 52011540403) and the Shanghai Pujiang Program (18PJ1405000). Peter K. Liaw thanks the support from the National Science Foundation (DMR-1611180 and 1809640) with the program directors, Drs. Judith Yang, Gary Shiflet, and Diana Farkas.

Appendices A. Experimental procedure

The model parameters were calibrated by the stress-strain curves obtained from a dog-bone cylindrical specimen with 16 mm gauge length, and 8 mm in diameter deformed under monotonic tension and compression along the RD. Similar specimen geometry had been used in our prior publications (Wu et al., 2014). The pure torsion and coupled torsion-tension loadings were realized by designing a square shape at each end of a thread-ended cylindrical specimen with 20 mm gauge length and 10 mm in diameter. The sample geometry was the same as that used in the published work (Guo et al., 2013).

The mechanical experiments were conducted on a customized MTS axial-torsional load frame at Vulcan Engineering Diffractometer, Spallation Neutron Source, Oak Ridge National Laboratory. Since the testing machine was a biaxial load frame, the experiments were controlled by displacement in the axial direction and the torsion angle in the circumferential direction, simultaneously. The deformation within the specimen gauge section was relatively uniform during the tests. The axial stress and strain were calculated based on the force and a 15% extensometer data in the axial direction. The shear stress and shear strain were determined by the torque and torsion angle. The force, axial strain, torque, and torsion angle were readily available in the MTS load frame. The load frame was capable of $100 \, \text{kN}$, and $400 \, \text{Nm}$ with 270° of rotation range. The system was calibrated by MTS on yearly basis to provide reliable data for general users from all over the world. Considering the sample geometry, the stress accuracy was in the order of $0.2 \, \text{MPa}$, and strain accuracy was in the order of 0.001%.

A.1. Rolled-sample under free-end torsion

Firstly, the torque was applied to the rolled-sample along the ND by increments of 2000 N \cdot mm at each step until a torque of 10,000 N \cdot mm was reached. The axial force was kept at 0 N. Next, the samples were twisted by increments of a torsion angle 14° at each step up to 56°. Samples were twisted to 60° in the last step. Finally, the samples were unloaded from 15,000 N \cdot mm by increments of 5000 N \cdot mm at each step until 0 N \cdot mm.

A.2. Rolled-sample under coupled torsion-tension

The torque was applied to the sample along the ND by increments of 2000 N · mm at each step until 10,000 N · mm was reached. At

the same time, the axial displacement increased by increments of 0.13 mm at each step. Next, the samples were twisted to a rotation angle of 20° . The rotation angle increased by increments of 10° at each step up to 60° . At the same time, the axial displacement increased by increments of 0.66 mm at each step. Finally, the samples were unloaded from 15,000 N·mm by increments of 5000 N·mm at each step to 0 N·mm. The axial displacement was unloaded correspondingly.

Appendix B. Comparison between measured and predicted twin volume fraction and deformed texture

The comparison between the predicted deformed textures and experimental textures available in literature under loading paths of tension, compression, and free-end torsion are shown in the Fig. B.1. Obviously, the predicted textures were in good agreement with the corresponding measured textures (Khan et al., 2011; Carneiro et al., 2021a) although the sample preparation and test conditions were not exactly the same. The comparison of the predictions for the twin volume fractions (TVFs) of our rolled-sample with the experimental results available in literature were shown in Fig. B.1g, the predicted TVFs under compression and free-end torsion showed similar increasing trends with the measured TVFs (Carneiro et al., 2021a). The consistency between the simulations and the available experiments demonstrates that the EVPSC-TDT model has a good predictability on the evolution of texture and twin volume fraction.

Appendix C. Mesh sensitivity study

All the numerical results presented in the current study are simulated with a mesh with 16 elements. Each element is a HEM consisted of 1784 orientations. To ensure the numerical results are not sensitive to the meshing size, the free-end torsion was simulated by the TFE-EVPSC-TDT model with 5 elements. Fig. C.1 compares the average shear stress, the average axial strain, and the stress distribution within the rod to those obtained with 16 elements. Obviously, the numerical results with 5 and 16 elements are nearly identical. In other words, the numerical results obtained with 16 elements in the current work are mesh insensitive and sufficiently accurate to predict the distribution of internal stress/strain.

References

Abdolvand, H., Daymond, M.R., Mareau, C., 2011. Incorporation of twinning into a crystal plasticity finite element model: evolution of lattice strains and texture in Zircaloy-2. Int. J. Plast. 27, 1721–1738.

Abdolvand, H., Daymond, M.R., 2012. Internal strain and texture development during twinning: comparing neutron diffraction measurements with crystal plasticity finite-element approaches. Acta Mater. 60, 2240–2248.

Abdolvand, H., Majkut, M., Oddershede, J., Schmidt, S., Lienert, U., Diak, B.J., Withers, P.J., Daymond, M.R., 2015. On the deformation twinning of Mg AZ31B: a three-dimensional synchrotron X-ray diffraction experiment and crystal plasticity finite element model. Int. J. Plast. 70, 77–97.

Agnew, S.R., Duygulu, O., 2005. Plastic anisotropy and the role of non-basal slip in magnesium alloy AZ31B. Int. J. Plast. 21, 1161-1193.

Agnew, S.R., Brown, D.W., Tomé, C.N., 2006. Validating a polycrystal model for the elastoplastic response of magnesium alloy AZ31 using *in situ* neutron diffraction. Acta Mater. 54, 4841–4852.

Albinmousa, J., Jahed, H., Lambert, S., 2011. Cyclic behaviour of wrought magnesium alloy under multiaxial load. Int. J. Fatigue 33, 1127-1139.

Andar, M.O., Kuwabara, T., Steglich, D., 2012. Material modeling of AZ31 Mg sheet considering variation of r-values and asymmetry of the yield locus. Mater. Sci. Eng. A 549, 82–92.

Balasuramanian, S., Anand, L., 2002. Plasticity of initially textured hexagonal poly-crystals at high homologous temperatures: application to titanium. Acta Mater. 50. 133–148.

Barnett, M.R., 2001. Influence of deformation condition and texture on the high temperature flow stress of magnesium AZ31. J. Light Met. 1, 167–177.

Barnett, M.R., 2007. Twinning and the ductility of magnesium alloys. Mater. Sci. Eng. A464, 1–7.

Beausir, B., Toth, L.S., Qods, F., Neale, K.W., 2009. Texture and mechanical behavior of magnesium during free-end torsion. J. Eng. Mater. Technol. 131, 011108. Bentachfine, S., Pluvinage, G., Toth, L.S., Azari, Z., 1996. Biaxial low cycle fatigue under non-proportional loading of a magnesium-lithium alloy. Eng. Fract. Mech. 54, 513–522.

Beyerlein, I.J., Tóth, L.S., 2009. Texture evolution in equal-channel angular extrusion. Prog. Mater. Sci. 54, 427–510.

Carneiro, L., Culbertson, D., Zhu, X.Y., Yu, Q., Jiang, Y.Y., 2021a. Twinning characteristics in rolled AZ31B magnesium alloy under three stress states. Mater. Charact. 175. 111050.

Carneiro, L., Culbertson, D., Yu, Q., Jiang, Y., 2021b. Twinning in rolled AZ31B magnesium alloy under free-end torsion. Mater. Sci. Eng. A 801, 140405.

Chapuis, A., Drivers, J.H., 2011. Temperature dependency of slip and twinning in plane strain compressed magnesium single crystals. Acta Mater. 59, 1986–1994. Cheng, Y., Fu, Y.J., Xin, Y.C., 2020. {10(1)over-bar2} twinning behavior under biaxial tension of Mg-3Al-1Zn plate. Int. J. Plast. 132, 102762.

Chino, Y., Sassa, K., Mabuchi, M., 2008. Enhancement of tensile ductility of magnesium alloy produced by torsion extrusion. Scr. Mater. 59, 399-402.

Clausen, B., Tomé, C.N., Brown, D.W., Agnew, S.R., 2008. Reorientation and stress relaxation due to twinning: modeling and experimental characterization for Mg. Acta Mater. 56, 2456–2468.

Culbertson, D., Yu, Q., Wang, J., Jiang, Y., 2017. Pre-compression effect on microstructure evolution of extruded pure polycrystalline magnesium during reversed tension load. Mater. Charact. 134, 41–48.

Dawson, P.R., Boyce, D.E., Park, J.S., Wielewski, E., Miller, M.P., 2018. Determining the strengths of HCP slip systems using harmonic analyses of lattice strain distributions. Acta Mater. 144, 92–106.

Eshelby, J.D., 1957. The determination of the elastic field of an ellipsoidal inclusion and related problems. Proc. R. Soc. Lond. A 241, 376-396.

Ganesan, S., Yaghoobi, M., Githens, A., Chen, Z., Daly, S., Allison, J.E., Sundararaghavan, V., 2021. The effects of heat treatment on the response of WE43 Mg alloy: crystal plasticity finite element simulation and SEM-DIC experiment. Int. J. Plast. 137, 102917.

Guo, X.Q., Wu, W., Wu, P.D., Qiao, H., An, K., Liaw, P.K., 2013. On the swift effect and twinning in a rolled magnesium alloy under free-end torsion. Scr. Mater. 69, 319–322.

Guo, X.Q., Wang, H., Qiao, H., Mao, X.B., 2015. Numerical study of the large strain behavior of extruded magnesium alloy AM30 tube by elastic viscoplastic self-consistent model. Mater. Des. 79, 99–105.

Hama, T., Takuda, H., 2012. Crystal plasticity finite-element simulation of work-hardening behavior in a magnesium alloy sheet under biaxial tension. Comput. Mater. Sci. 51, 156–164.

- Hong, S.G., Park, S.H., Lee, C.S., 2010. Enhancing the fatigue property of rolled AZ31 magnesium alloy by controlling {10-12} twinning-detwinning characteristics. J. Mater. Res. 25, 784–792.
- Huang, X.S., Suzuki, K., Watazu, A., Shigematsu, I., Saito, N., 2008. Mechanical properties of Mg–Al–Zn alloy with a tilted basal texture obtained by differential speed rolling. Mater. Sci. Eng. A488, 214–220.
- Indurkar, P.P., Baweja, S., Perez, R., Joshi, S.P., 2020. Predicting textural variability effects in the anisotropic plasticity and stability of hexagonal metals: application to magnesium and its alloys. Int. J. Plast. 132. 102762.
- Kang, J.Y., Bacroix, B., Brenner, R., 2012. Evolution of microstructure and texture during planar simple shear of magnesium alloy. Scr. Mater. 66, 654-657.
- Khan, A.S., Pandey, A., Gnäupel-Herold, T., Mishra, R.K., 2011. Mechanical response and texture evolution of AZ31 alloy at large strains for different strain rates and temperatures. Int. J. Plast. 27, 688–706.
- Lebensohn, R.A., Tomé, C.N., 1993. A self-consistent anisotropic approach for the simulation of plastic deformation and texture development of polycrystals-application to zirconium alloys. Acta Metall. Mater. 41, 2611–2624.
- Lebensohn, R.A., Tomé, C.N., Ponte Castañeda, P., 2007. Self-consistent modeling of the mechanical behavior of viscoplastic polycrystals incorporating intragranular field fluctuations. Philos. Mag. 87, 4287–4322.
- Lou, X.Y., Li, M., Boger, R.K., Agnew, S.R., Wagoner, R.H., 2007. Hardening evolution of AZ31B Mg sheet. Int. J. Plast. 23, 44–86.
- Ma, C., Wang, H., Hama, T., Guo, X.Q., Mao, X.B., Wang, J., Wu, P.D., 2019. Twinning and detwinning behaviors of commercially pure titanium sheets. Int. J. Plast. 121, 261–279.
- Masson, R., Bornert, M., Suquet, P., Zaoui, A., 2000. An affine formulation for the prediction of the effective properties of nonlinear composites and poly-crystals. J. Mech. Phys. Solids 48, 1203–1227.
- Neale, K.W., Toth, L.S., Jonas, J.J., 1990. Large strain shear and torsion of rate-sensitive FCC polycrystals. Int. J. Plast. 6, 45–61.
- Oppedal, A.L., El Kadiri, H., Tomé, C.N., Vogel, S.C., Horstemeyer, M.F., 2011. Anisotropy in hexagonal close-packed structures: improvements to crystal plasticity approaches applied the magnesium alloy. Philos. Mag. 93, 4311–4330.
- Paramatmuni, C., Dunne, F.P.E., 2020. Effect of twin crystallographic orientation on deformation and growth in Mg alloy AZ31. Int. J. Plast. 135, 102775.
- Pollock, T.M., 2010. Weight loss with magnesium alloys. Science 328, 986-987.
- Popova, E., Staraselski, Y., Brahme, A., Mishra, R.K., Inal, K., 2015. Coupled crystal plasticity–probabilistic cellular automata approach to model dynamic recrystallization in magnesium alloys. Int. J. Plast. 66, 85–102.
- Proust, G., Tomé, C.N., Kaschner, G.C., 2007. Modeling texture, twinning and hardening evolution during deformation of hexagonal materials. Acta Mater. 5, 137–2148.
- Proust, G., Tomé, C.N., Jain, A., Agnew, S.R., 2009. Modeling the effect of twinning and detwinning during strain-path changes of magnesium alloy AZ31. Int. J. Plast. 25, 861–880.
- Qiao, H, Guo, P.D, Oppedal, A.L., El Kadiri, H., Wu, P.D., Agnew, S.R., 2017. Twin-induced hardening in extruded Mg alloy AM30. Materials Science and Engineering A 687, 17–27.
- Qiao, H., Wu, P.D., Wang, H., Gharghouri, M.A., Daymond, M.R., 2015. Evaluation of elastic-viscoplastic self-consistent polycrystal plasticity models for zirconium allovs. Int. J. Solids Struct. 71, 308–322.
- Sahoo, S.K., Biswas, S., Toth, L.S., Gautam, P.C., 2020. Strain hardening, twinning and texture evolution in magnesium alloy using the all twin variant polycrystal modelling approach. Int. J. Plast. 128, 102660.
- Simmons, G., Wang, H., 1971. Single Crystal Elastic Constants and Calculated Poly-Crystal Properties. MIT Press, Cambridge.
- Song, B., Wang, C., Guo, N., Pan, H., Xin, R., 2017. Improving tensile and compressive properties of an extruded AZ91 rod by the combined use of torsion deformation and aging treatment. Materials 10 (3), 280.
- Steglich, D., Jeong, Y., Andar, M.O., Kuwabara, T., 2012. Biaxial deformation behavior of AZ31 magnesium alloy: crystal-plasticity-based prediction and experimental validation. Int. J. Solids Struct. 49, 3551–3561.
- Sun, J., Jin, L., Dong, J., 2019. Towards high ductility in magnesium alloys the role of intergranular deformation. Int. J. Plast. 123, 121–132.
- Swift, H.W., 1947. Length changes in metals under torsional overstrain. Engineering 163, 253–257.
- Tang, T., Zhou, G., Li, Z., Li, D., Peng, L., Peng, Y., Wu, P.D., Wang, H., Lee, M.G., 2019. A polycrystal plasticity based thermo-mechanical-dynamic recrystallization coupled modeling method and its application to light weight alloys. Int. J. Plast. 116, 159–191.
- Van Houtte, P., 1978. Simulation of the rolling and shear texture of brass by the Taylor theory adapted for mechanical twinning. Acta Mater. 26 (4), 591-604.
- Van der Giessen, E., 1987. FE-thermomechanics and material sampling points. Comput. Methods Appl. Mech. Eng. 64, 447–465.
- Wang, H., Wu, Y., Wu, P.D., Neale, K.W., 2010a. Numerical analysis of large strain simple shear and fixed-end torsion of HCP polycrystals. CMC-Computers. Mater. Contin. 19, 255–284.
- Wang, H., Raeisinia, B., Wu, P.D., Agnew, S.R., Tomé, C.N., 2010b. Evaluation of self-consistent polycrystal plasticity models for magnesium alloy AZ31B sheet. Int. J. Solids Struct. 47, 2905–2917.
- Wang, H., Wu, P.D., Tomé, C.N., Huang, Y., 2010c. A finite strain elastic-viscoplastic self-consistent model for polycrystalline materials. J. Mech. Phys. Solids 58, 594–612.
- Wang, H., Wu, P.D., Tomé, C.N., Wang, J., 2012a. A constitutive model of twinning and detwinning for HCP polycrystals. Mater. Sci. Eng. A555, 93-98.
- Wang, H., Wu, P.D., Tomé, C.N., Wang, J., 2012b. Study of lattice strains in magnesium alloy AZ31 based on a large strain elastic-viscoplastic self-consistent polycrystal model. Int. J. Solids Struct. 49, 2155–2167.
- Wang, H., Wu, P.D., Wang, J., 2013a. Modeling inelastic behavior of magnesium alloys during cyclic loading-unloading. Int. J. Plast. 47, 49–64.
- Wang, H., Wu, P.D., Wang, J., Tomé, C.N., 2013b. A crystal plasticity model for hexagonal close packed (HCP) crystals including twinning and de-twinning mechanisms. Int. J. Plast. 49, 36–52.
- Wang, H., Wu, P.D., Wang, J., 2015a. Modelling the role of slips and twins in magnesium alloys under cyclic shear. Comput. Mater. Sci. 96, 214-218.
- Wang, H., Wu, P.D., Wang, J., 2015b. Numerical assessment of the role of slip and twinning in magnesium alloy AZ31B during loading path reversal. Metall. Mater. Trans. 46A, 3079–3090.
- Wang, H., Clausen, B., Capolungo, L., Beyerlein, I.J., Wang, J., Tomé, C.N., 2016a. Stress and strain relaxation in magnesium AZ31 rolled plate: in-situ neutron measurement and elastic viscoplastic polycrystal modeling. Int. J. Plast. 79, 275–292.
- Wang, H., Lee, S.Y., Gharghouri, M.A., Wu, P.D., 2016b. Deformation behavior of Mg-8.5wt.%Al alloy under reverse loading investigated by in-situ neutron diffraction and elastic viscoplastic self-consistent modeling. Acta Mater. 107, 404–414.
- Wang, H., Wu, P.D., Kurukuri, S., Worswick, M.J., Peng, Y.H., Tang, D., Li, D.Y., 2018. Strain rate sensitivities of different deformation mechanisms of magnesium alloys. Int. J. Plast. 107, 207–222.
- Wang, H., Lee, S.Y., Huang, E.W., Jain, J., Li, D.Y., Peng, Y.H., Choi, H.S., Wu, P.D., 2020a. Crystal plasticity modeling and neutron diffraction measurements of a magnesium AZ31B plate: effects of plastic anisotropy and surrounding grains. J. Mech. Phys. Solids 135, 103795.
- Wang, Y., Culbertson, D., Jiang, Y., 2020b. An experimental study of anisotropic fatigue behavior of rolled AZ31B magnesium alloy. Mater. Des. 186, 108266.
- Wu, L., Jain, A., Brown, D.W., Stoica, G.M., Agnew, S.R., Clausen, B., Fielden, D.E., Liaw, P.K., 2008. Twinning-detwinning behavior during the strain-controlled low-cycle fatigue testing of a wrought magnesium alloy, ZK60A. Acta Mater. 56, 688–695.
- Wu, P.D., Van der Giessen, E., 1991. Analysis of elastic-plastic torsion of circular bars at large strains. Arch. Appl. Mech. 61, 89-103.
- Wu, P.D., Wang, H., Neale, K.W., 2012. On the large strain torsion of HCP polycrystals. Int. J. Appl. Mech. 4, 1250024.
- Wu, W., Qiao, H., An, K., Guo, X.Q., Wu, P.D., Liaw, P.K., 2014. Investigation of deformation dynamics in a wrought magnesium alloy. Int. J. Plast. 62, 105–120.
- Xin, R., Liu, Z., Sun, Y., Wang, H., Guo, C., Ren, W., Liu, Q., 2019. Understanding common grain boundary twins in Mg alloys by a composite Schmid factor. Int. J. Plast. 123, 208–223.
- Xiong, Y., Yu, Q., Jiang, Y., 2012. Multiaxial fatigue of extruded AZ31B magnesium alloy. Mater. Sci. Eng. A546, 119–128.

- Zecevic, M., Lebensohn, R.A., McCabe, R.J., Knezevic, M., 2019. Modelling recrystallization textures driven by intragranular fluctuations implemented in the viscoplastic self-consistent formulation. Acta Mater. 164, 530–546.
- Zhang, J., Yu, Q., Jiang, Y., Li, Q., 2011. An experimental study of cyclic deformation of extruded AZ61A magnesium alloy. Int. J. Plast. 27, 768-787.
- Zhang, M.J., Zhang, H., Ma, A.X., LLorca, J., 2021a. Experimental and numerical analysis of cyclic deformation and fatigue behavior of a Mg-RE alloy. Int. J. Plast. 139, 102885.
- Zhang, X.D., Li, S.M., Guo, X.Q., Wang, H., Yu, Q., Wu, P.D., 2021b. Effects of texture and twinning on the torsional behavior of magnesium alloy solid rod: a crystal plasticity approach in comparison with uniaxial tension/compression. Int. J. Mech. Sci. 191, 106062.
- Zhou, G.W., Jain, M.K., Wu, P.D., Shao, Y.C., Li, D.Y., Peng, Y.H., 2016. Experimental and crystal plasticity analysis on plastic deformation of AZ31B Mg alloy sheet under intermediate temperatures: how deformation mechanisms evolve. Int. J. Plast. 79, 19–47.